A paleomagnetic study of the angrite Sahara 99555

by

Sarah P. Slotznick

Submitted to the Department of Earth, Atmospheric and Planetary Sciences

in Partial Fulfillment of the Requirements for the Degree of

Bachelor of Science in Earth, Atmospheric and Planetary Sciences

at the Massachusetts Institute of Technology

May 26, 2009 [June 2009]

Author Signature redacted
Department of Earth, Atmospheric and Planetary Sciences
May 8, 2009

Certified by Signature redacted
Benjamin Weiss
Thesis Supervisor

Accepted by Signature redacted
Samuel Bowring
Chair, Committee on Undergraduate Program

Contents

Abstract

Sahara 99555 (SAH 99555) is the oldest dated angrite sample, a rare type of meteorite, and is only ~2 Myr younger than the age of the solar system *(1, 2).* SAH 99555 shows no post-cooling brecciation or weathering from the parent body, and does not display signs of significant terrestrial weathering. Therefore, paleomagnetic experiments were conducted for the first time on SAH 99555 to discover if it contains a primary paleomagnetism and then to determine a paleointensity estimate and its ferromagnetic mineralogy. Our studies show that the primary ferromagnetic mineral in SAH 99555 is magnetite and there are also some accessory ferromagnetic minerals including titanomagnetite and hematite. The natural remanent magnetization (NRM) of SAH 99555 appears to have a low-coercivity component probably from a collector's hand magnet or the Earth's field as well as a high-coercivity component, similar to D'Orbigny, another angrite. The paleointensity measurements of the high-coercivity component of SAH 99555,5 agree with the paleointensity estimates made for other angrites (D'Orbigny and A-881371) by Weiss et al. (2008) *(4).* Therefore, it appears that SAH 99555 does record a primary paleofield from when it was on the angrite parent body, which would be the oldest known paleomagnetic record yet identified in a planetary rock. Further studies are suggested to verify these conclusions, which make SAH 99555 one more key data point in the understanding of the early solar system.

Acknowledgements

I would like to thank Benjamin Weiss for his teaching and guidance throughout this entire thesis process.

I would also like to thank Nilanjan Chatterjee for his incredible help with collecting the electron microscopy data, Sonia Tikoo, Jennifer Buz, Ian Garrick-Bethel, and Laurent Carporzen for answering questions about lab protocol and software, and Jane Connor for her guidance toward getting the thesis process started and keeping me on track throughout the process.

Lastly, I would like to thank my family and friends for being supportive throughout the year as I worked on my research.

Introduction

Angrites are a rare type of achrondritic meteorite with only 17 known samples on the earth. From an as yet unknown parent body, angrites are some of the oldest known rocks in the solar system, with Pb/Pb ages of 4565-4558 Ma *(1, 2)*. The oldest angrites are only ~2 Myr younger than the minimum age of the solar system at 4.5672 Gyr, which is found by dating calcium-aluminum rich inclusions (CAIs) *(3)*. Unlike many other achondrites, angrites are not shocked from meteoroid impacts on the parent body and show no signs of post-cooling brecciation or weathering from the parent body (which can change both the chemistry of the meteorite and modify or potentially reset the magnetization) *(4)*. They therefore contain some of the best preserved records of the early solar system.

Angrites are interpreted to be mafic igneous rocks from a differentiated planetesimal. The group is identified by their unique oxygen-isotope composition and unusual mineral assemblages *(5)*. Mainly basaltic [with the exception being the cumulate or partially crystallized Angra dos Reis*(6)*], they fall into two major groupings: the quickly cooled "quenched" angrites (which include SAH 99555, D'Orbigny and A-881371) and the "slowly cooled" angrites (which include Angra dos Reis) *(7)*.

All of the studied angrites contain ferromagnetic minerals and therefore could have potentially recorded paleomagnetic fields from the angrite parent body. Specifically, angrites often contain several primary ferromagnetic minerals: low-Ti magnetite *(8)*, titanomagnetite (typically with a composition of 71-77% ulvöspinel i.e. TiO_2 of 25-27%) *(9)* and rarer kamacite and pyrrhotite *(9, 10)*. Although magnetic fields can be generated by large impacts, the lack of brecciation and shock on the angrites suggests they are unlikely to have been magnetized by

such processes. Therefore, any paleomagnetic record on the angrites could be from either of the two field-generating mechanisms postulated to have been active during the early solar system: an external stellar and circumstellar disk field and an internal core dynamo on the angrite parent body (APB). Of the twelve known angrites, NWA 2999 and NWA 4801 had their primary magnetization overprinted by collector's hand magnets. NWA 4931 was heavily weathered on Earth and therefore probably does not record a primitive magnetic field. Three of the remaining angrites (Angra dos Reis, D'Orbigny, and A-881371) have undergone paleomagnetic experiments which suggested internal field generation through a core dynamo on the APB *(4)*.

Basic Paleomagnetism Theory

Many rocks contain ferromagnetic minerals which can be magnetized. Single domain (SD) grains (which are very small, often with $d < 0.1$ μm) will magnetize in one direction and therefore are good carriers of remanent magnetization. Multi-domain (MD) grains ($d > 1$ μm) can have several different moments depending on the domain. In addition, these fields decay faster with time (due the presence of domain walls), so they are less effective as recorders of paleofields. Pseudo single domain (PSD) grains fall between the two other types. They remain relatively stable in time and have relatively high coercivity. Coercivity is the intensity of the magnetic field needed to entirely demagnetize a sample after it has been saturated. (Large coercivities mean the material is less easily remagnetized.) Therefore, pseudo single domain grains are also important in paleomagnetic studies.

Hysteresis loops explain the general process of magnetization of a rock (Fig. 1). Originally the magnetization directions of the ferromagnetic minerals are pointing in many different directions, each along the elongated/"easy" axis of the SD grain. As an external magnetic field is applied to the rock, the magnetic moments of the grains will align with this external field. Once the field is removed the moments snap back to the nearest long axis, resulting in a remanent magnetization being preserved within the rock. Multiple domain grains follow the same basic concept, although their overall magnetization is different due to domain walls within the grain.

Natural remanent magnetization (NRM) is any remanent magnetization in a rock before laboratory analysis. This include primary NRM, which is the component of the NRM vector acquired during rock formation, as well as secondary NRM which is any magnetization acquired after rock formation. Of the three types of primary NRM, we are most concerned with thermoremanent magnetization (TRM) in this experiment as it is the form acquired by igneous rocks (Fig. 2). TRM occurs when a rock cools from above its Curie temperature in the presence of an external magnetic field. In the example of a basalt, non-magnetic crystals will start to form when the lava is very hot and far above the Curie temperature. Below the Curie temperature, certain minerals will acquire moments (become ferromagnetic), but these moments will continually flip directions depending on the applied external field. Once the lava cools below the blocking temperature, the moments become fixed and stable, resulting in a TRM *(11)*.

The NRM of a rock can be measured by slowly demagnetizing a sample and measuring how the moment decreases as it demagnetizes. There are two main laboratory methods for

demagnetization: alternating field (AF) demagnetization and thermal demagnetization. For thermal demagnetization, the sample is heated up to a temperature below the Curie point and then cooled in a zero field. Any ferromagnetic grains with a blocking temperature below this value will be demagnetized. For AF demagnetization, a decaying alternating magnetic field is applied to the sample which effectively erases any magnetization with a coercivity less than the peak intensity of the applied field. In this manner, the NRM of the sample can be measured and can be used to determine the intensity of the applied field which produced the magnetization recorded in the rock.

Sahara 99555

Sahara 99555 (SAH 99555) was found in 1999 in the Sahara desert. With a total weight of 2.71 kg, it is the second largest recovered angrite to date. It has a Pb-Pb age of between 4564.58 to 4564.86 Ma *(12, 2)* which is slightly older than the Pb-Pb age of D'Orbigny of 4564.42 Ma *(1)* (making SAH 99555 the oldest dated angrite and in fact the oldest known unshocked igneous rock!) The ^{53}Mn-^{53}Cr relative ages of these two samples are very close as well, although when converted to absolute ages they are slightly younger than those found by Pb-Pb dating *(7)*. The cosmic ray exposure age of SAH 99555 is around 6 Ma, which is within the uncertainty of the exposure age of A-881371, so they could potentially be from the same ejection event *(13, 14)*.

SAH 99555 is a fine-grained igneous rock with basaltic texture. It is mainly composed of olivine (including kirschsteinite), fassaitic clinopyroxene, and anorthite with minor phases including titanomagnetite, troilite, an unknown silicophosphate phase, and traces of a FeNi-

metal. Compositionally, SAH 99555 and D'Orbigny are almost identical, the only set angrites found so far to share the same geochemistry *(5)*. SAH 99555 has a complex intergrowth texture of plagioclase laths (almost pure anorthite) and olivine *(14, 15)*. The titanomagnetite is 0.7 vol. percent of the total rock as found by point-counting technique *(14)*. The titanomagnetite in SAH 99555 was found to have a composition of 25-27 wt% TiO_2 and 1.5 wt% Al_2O_3 *(15)*. Therefore the chemical formula is $Fe_{2.1}$ $Ti_{0.7}$ O_4 and the predicted Curie point of the titanomagnetite is 130°C *(16)*. Enrichments of light rare earth elements in SAH 99555 indicate that there is evidence of slight terrestrial alteration of SAH 99555 (17). However, this chemical alteration was not visible by thin section (see also our data below) *(18)*.

No paleomagnetic studies have been published yet on SAH 99555. However since it is a desert meteorite, it is quite possible that it has been remagnetized by a collector's hand magnet. The purpose of this study is to perform the first *ever* magnetic experiments on SAH 99555 to discover if it contains a primary paleomagnetism, and then perform paleointensity experiments (to determine the strength of that field) and determine its ferromagnetic mineralogy. This will provide another key data point for understanding the early solar system and the APB, and pave the way for future studies to do more intensive experimentation.

Electron Microscopy Study

Although previous petrological studies have been done on SAH 99555 *(14, 13)*, these studies have not focused on the ferromagnetic minerals which are less than 1% volume of the sample. In fact, both Floss et al. (2003) *(15)* and Mikouchi et al. (2000) *(14)* used backscatter electron microscopy imaging and published back-scatter electron (BSE) photographs. Neither

of these BSE studies imaged the ferromagnetic mineral (identified as titanomagnetite in these papers). Therefore, we conducted an electron microscopy study to: (a) determine the precise composition and identity of the ferromagnetic minerals, and (b) determine whether these minerals are preterrestrial or the product of weathering on Earth.

After AF demagnetization and rock magnetic studies were conducted on a small sample cut from SAH 99555 labeled SAH 99555,5, this piece was broken into 4 pieces using nonmagnetic tools (Fig. 3). Sample ,5b, a 55 mg piece, was then mounted by cyanoacrylate cement onto a quartz disk. It was polished using aluminum oxide polishing paper and then silicon oxide paper. After being cleaned with ethanol, the entire quartz disk and sample were carbon coated using a Denton vacuum carbon coater. Backscatter electron microscopy imaging combined with quantitative wavelength dispersive spectroscopy analysis were used to determine the basic mineralogy of the sample.

Our results indicate that SAH 99555 contains kirschsteinite, anorthite, and fassaitic clinopyroxene (Fig. 4), a finding consistent with previous studies *(14, 15)*. Small percentages of troilite were found, often associated with ferromagnetic minerals containing Ti and Fe. In addition, a Ca-phosphate phase and a very small amount of metal (part per million scale), which was identified as palladium, were found. A complex intergrowth pattern exists between anorthite and the olivine (Fig. 5). The olivine was visibly zoned, indicative of rapid cooling. Between two crystals of troilite and fassaitic clinopyroxene, a reaction front was seen along the grain boundary in the form of a small grain of clinopyroxene with an increased % of iron. The ferromagnetic minerals were always found near troilite crystals; however, there did not appear

to be much alteration of the Fe-Ti oxide (ferromagnetic crystals). These oxides appeared relatively unweathered.

Quantitative wavelength dispersive spectroscopy was conducted on 5 different crystals of the large iron-titanium oxide mineral scattered across the sample, and all had very similar chemical compositions (Table 1). Although SAH 99555,5b was tested for Fe, Ti, and Al cations, no distinction was made between ferrous and ferric iron. However, chemical balancing using the atomic masses (Table 2) gave the following oxide weight percents which were only slightly different than those previously published *(14)*: 54-61 wt% FeO, 10-18 wt% Fe_2O_3, 21-26 wt% TiO_2, and 2.5-4 wt% Al_2O_3. By looking at the atomic proportions, it appears to plot between the ilmenite-hematite series and ulvöspinel-magnetite series on the FeO-Fe_2O_3-TiO_2 system (Fig. 6). However, it is much closer to the titanomagnetite series and has an approximate formula of $Fe_{2.26}Ti_{.74}O_4$ (assuming the aluminum is an impurity substituting for ferric iron.)

Since the composition plots halfway between titanomagnetite and titanohematite, this could be a sign of terrestrial alteration. Titanohematite and titanomaghemite are normally terrestrial weathering minerals. In fact, titanomaghemite forms from the oxidation of titanomagnetite *(19)*. However, as mentioned before, this ferromagnetic mineral appeared relatively unweathered and the signs of titanomaghemite including more fractures and mottled colors *(20)* were not present. Therefore, although some terrestrial alteration and weathering may have occurred, it does not appear to have been to a great extent.

In addition to the relatively large unweathered grains of titanomagnetite, there were small percentages of other Fe-Ti oxides in the sample. In small rims around the troilite (Fig. 7), there were some cases of Fe-Ti-Al oxides which also lie between the ilmenite-hematite series

and the ulvöspinel-magnetite series (Fig. 8). It appears that one of the grains studied is more similar to titanomagnetite while the other is closer to hematite. These grains have formulas ranging from $Fe_{2.66}Ti_{0.34}O_4$ to $Fe_{2.49}Ti_{0.34}O_4$ (assuming the aluminum is an impurity substituting for ferric iron.) (Table 2) These low-Ti oxides are much less frequent than the high-Ti titanomagnetite described above. However, due to their appearance around the grain boundaries, it is possible these oxides are displaying the result of terrestrial alteration.

Three iron-oxide grains were found with little to no Ti or Al (Table 1, Fig. 9). These contain a range of wt% FeO v. Fe_2O_3 (i.e. ferric v. ferrous oxide). When plotted on the ternary diagram (Fig. 8), one can see that A is magnetite (38 wt% FeO), B is hematite (21 wt% FeO), and C is almost exactly between magnetite and hematite (24 wt% FeO). The most important note is that the hematite grain found is right next to the magnetite (Fig. 9).

Magnetite is the primary ferromagnetic mineral in D'Orbigny (as well as A-881371) *(4)* which SAH 99555 is very similar to compositionally. This suggests that magnetite could be the primary ferromagnetic mineral in SAH 99555. However, the fact that the hematite is found right next to the magnetite suggests terrestrial alteration may have occurred and altered the primary ferromagnetic mineral. This would greatly affect the paleomagnetic studies on the sample. Therefore, other techniques must be used to determine more precisely to what extent alteration affected the magnetite (as well as the other ferromagnetic minerals) and to determine which of the ferromagnetic minerals is primary.

VSM Experiment

In order to gather more data on the crystal size as well as the ferromagnetic mineralogy, measurements were done on a subsample SAH 99555,5c using a Digital Measurement Systems vibrating sample magnetometer (VSM) in C. Ross's laboratory at MIT. SAH 99555,5c (weighing 19 mg) was mounted on a quartz rod using silver glue for loading into the VSM.

Hysteresis loops at room temperature were measured to help determine limits on the saturation magnetization field and domain size (SD v. PSD v. MD). Fields from -10,000 G to 10,000 G were applied to the sample in steps of 500 G and 50 G (from -500 G to 500 G). Then the steps were reversed from 10,000 G to -10,000 G. The high-field slope of each hysteresis loop was used as an estimate of the paramagnetic susceptibility (i.e., contribution of paramagnetic minerals to the hysteresis loop.) This high-field slope was then subtracted from the data to form hysteresis loops (Fig. 10). From the hysteresis loop for SAH 99555,5c, we were able to determine other parameters such as the saturation moment, saturation remanent moment, and the coercivity (Table 3). These values (and the hysteresis loops themselves) are very similar to those of D'Orbigny and A-881371 *(4)*, falling within the range of values from D'Orbigny samples and often the very close to the A-881371 sample. Following the method by Dunlop *(21)*, the ratios of saturation remanent magnetization to saturation magnetization (M_{rs}/M_s) and the coercivity of remanence to coercivity (H_{cr}/H_c) were calculated to find a boundary on the domain size. These ratios plot along the single domain-multiple domain mixing line, which simulates pseudo-single domain crystals, on a Day plot (M_{rs}/M_s v. H_{cr}/H_c) for magnetite (believed to be the ferromagnetic mineral.) D'Orbigny and A-881371 plot in a similar location and are interpreted to have PSD grains while Angra dos Reis has a superparamagnetic

grain component in one of the samples *(4)*. In summary, the rock magnetic properties of SAH 99555 are consistent with magnetite, and not hematite, being the dominant ferromagnetic mineral. They are in fact indistinguishable from the petrologically similar angrite D'Orbigny which itself is essentially unweathered. Therefore, the rock magnetic data strongly suggest that the paleomagnetic record of SAH 99555 is unlikely to be primarily the product of terrestrial weathering.

Paleomagnetic Experiments

The sample of SAH 99555 obtained by the MIT Paleomagnetism Laboratory was located on the outside of the meteorite as noted by the fusion crust on one of the uncut surfaces. (The sample contained two perpendicular cut surfaces) A 132 mg piece named SAH 99555,5 was cut using a non-magnetic precision wafering saw from this larger piece measuring about 6 mm by 4 mm by 1 mm (Fig. 11). This subsample came from the innermost part of the sample, furthest from the surface containing the fusion crust (about 1 cm away from this outer surface). Careful photographic records allowed this piece to be mutually oriented with the rest of the sample to within 5 degrees. Also the natural remnant magnetization (NRM) of all the samples were measured before and after any cut and a vector sum of the moments was calculated. This vector sum of the subsamples was compared with the parent sample to verify that the sawing process did not magnetize the samples. SAH 99555,5 was mounted with cyanoacrylate cement onto a quartz disk for the paleomagnetic experiments. Nearly all handling of the sample was done inside a class 10,000 clean laboratory within a larger magnetically shielded room (DC field <150 nT).

All of the paleomagnetic measurements were done in the MIT Paleomagnetism Laboratory with a 2G Enterprises Superconducting Rock Magnetometer 755 within the magnetically shielded room. With the use of an automatic sample handler, the magnetometer ran a high-resolution automated protocol of alternating field (AF) demagnetization steps and rock magnetization experiments. All of these experiments were non-destructive (as opposed to thermal demagnetization experiments), and therefore the same sample could be used for multiple experiments.

AF Demagnetization

Methods

Using the magnetometer, fields were applied in three axes at small increasing increments until the sample was totally demagnetized of any previous NRM. At this point any moments left were artificial and due to anhysteric remnant magnetization (ARM) induced by the system or gyromagnetic remnant magnetization (GRM) [see Weiss et al. 2008 *(4)* for details.] Specifically fields were applied increasingly in steps of 5 G starting at 15 G until 200 G; then they were applied with increasing intervals of 10 G until 850 G. Beyond this level, the magnetometer is only able to do uniaxial measurements so the field was applied only in one direction for z-axis demagnetization in steps of 40 G until 2900 G. While executing the AF demagnetization procedure, the magnetometer also tested the sample for GRM by performing uniaxial AF demagnetization in each of the three orthogonal axes. These measurements were then combined to form a vector which was compared to the NRM vector at the same AF demagnetization level to see if any artificial GRM was present in the meteorite. The GRM

measurements were taken at every 100 G as well as at 15 G (the starting point) and 850 G (when GRM measurements stopped.) After the data was collected from the demagnetization process, sets of the steps were averaged to reduce noise from ARM in the results. Using MATLAB, block averaging was done for group of 5 and 10 AF steps while moving averaging was done for sets of 5 steps. (A block average is a normal average with the sum of the steps and division by the # of steps added. A moving average is when the first step is averaged with the second step, then the third step is averaged with this result, etc.)

Results and Discussion

During the experiment, it was discovered that the rod holding the sample was not tight, and was slowly rotating as the automated process continued with each measurement. This discovery was made at AF level 280 G, and at the point the sample had rotated about 40° counterclockwise from its original orientation. However, due to way in which the sample was mounted on the slide (with top facing up), this only affected the declination of the sample. At step 280 G, the machine was stopped, the problem was fixed, and the rest of the run occurred with the sample reoriented to its original position.

When the GRM uniaxial measurements were added, the resulting vectors were always very close to the NRM of the sample at the same level (Table 4). Therefore artificial GRM was not a factor in the remanent magnetization of the sample.

In the orthographic projection of the moment of SAH 99555,5 (Fig. 12), the smooth decrease of declination and inclination toward the origin demonstrates the gradual demagnetization of the sample. At AF level 140 G, most of the magnetization has been

removed and the remaining points are in a large cluster. As noted above, the sample was rotating up to step 280 G. Therefore, it is quite probable that the plotted measurements of the decreasing moment are not in the correct position. (Hypotheses of the actual magnetization in this range will be discussed in greater detail in connection with the equal area plots later in this report.)

The large cluster of points around the origin is difficult to interpret due to its noisy nature. However, when the averaging technique is used, much of the noise disappears (Fig. 13). The averaging technique was only applied to the measurements taken above 280 G due to the potential errors in the other data. When studying the data points of the block averaging of 5 steps, a pattern emerges from the large cluster, and one can follow the moment of the sample toward the origin as it continues to demagnetize all the way up to 2900 G. The 10-step block averaging shows the same pattern, but with less detail. Using a block average appears to be a better method of averaging than the moving average, as the pattern decreasing to the origin is much clearer on the 5-step block average plot than the moving average plot.

The equal area plot (Fig. 14) also improved by using the 5-step block averaging, and the moments form a distinct group that was not possible to see with all the data points. One may also note that the measurements of levels below AF 280 G are similarly clustered, but are separated from the correctly oriented measurements above AF 280 G. Due to the slightly incorrect change in declination each time, this cluster formed instead of a smooth transition. However, one can still interpret the data since the original data points/first few measurements had not moved greatly. There is a clear 90° change in magnetization direction as the NRM measurements for these first AF steps are mainly in the upper hemisphere to the south. The

measurements after 280 G are all to the west with slightly more in the lower hemisphere. This suggests that a large change in direction occurred in the NRM below 280 G, which is indicative of a low-coercivity component of the magnetization. A similar "overprinting" phenomenon was found in D'Orbigny by Weiss et al. *(4)* where a low-coercivity component was visible up to about 50 G to 100 G before it disappeared. This low-coercivity component was hypothesized to come from a collector's hang magnet.

These results suggest that like D'Orbigny, the NRM of SAH 99555,5 displays two components: the low-coercivity secondary NRM that is likely a recent overprint (either from a hand magnet or the Earth's field) and another high-coercivity component. The latter is probably primary and not the result of a collector's magnet since the data points on the orthographic plots move gradually to the origin in the same general direction with decreasing sized steps with increasing levels of AF. However, since the actual sudden change in direction of the magnetic moment vector (the most indicative sign of overprinting) is smoothed into a curve by the rotation at low AF levels, further tests should be done to verify this conclusion.

ARM and IRM

Methods

After the NRM had been removed from the sample using AF demagnetization, another suite of paleomagnetic experiments were performed on it. First, SAH 99555,5 was given anhysteric remanent magnetization (ARM) by applying increasing DC bias fields in steps 2 G up to 20 G while in a peak AC field of 2000 G. These measurements can be used to determine the amount of magnetostatic interactions (interactions between the individual magnetic fields

produced by each ferromagnetic grain) within the sample *(22)*. This ARM was then AF demagnetized in small steps from 15 G to 2020 G. Next, the sample was given isothermal remanent magnetization (IRM) with a DC field of 2000 G which was also AF demagnetized using the same steps as the ARM AF demagnetization. Next, IRM acquisition was tested in the sample by applying increasing fields of IRM to the sample from 46 G to 8865 G, at which point saturation remanent magnetization would definitely be attained. IRM acquisition and AF demagnetization of IRM indicate the coercivity spectrum of the sample *(4)*. Using this data, the Lowrie-Fuller test, which indicates grain size and stress state, was performed by comparing the AF demagnetization of ARM and IRM *(23, 24)*.

Results and Discussion

The numerical results are summarized in Table 5. ARM acquisition results (Fig. 15) show that SAH 99555 has highly interacting grains, which is very similar to D'Orbigny and A-881371. The mean destructive field for an ARM with a 20 G DC bias field acquired in a 2000 G AC field is 17.3 mT within the range of values found for both D'Orbigny and Angra dos Reis (Table 5). The Lowrie-Fuller Test shows that SAH 99555 is a high-field type where the IRM is more stable than the ARM (Fig. 16). This is similar to the two other "quenched" angrites (quickly cooled since basaltic) tested, but is different than Angra dos Reis, which is thought to be slowly cooled, and has a low-field type behavior.

When looking at the IRM acquisition and demagnetization data (Fig. 17), it is clear that once again SAH 99555 is similar to D'Orbigny and A-881371, but very different than Angra dos Reis. Combined with the calculated values from this data [S-ratios *(25-27)* and coercivity of

remanence values], it is clear that SAH 99555 has a unimodal coercivity spectrum indicating one main ferromagnetic mineral within a similar range of coercivities as D'Orbigny and A-881371 [whose main ferromagnetic mineral is low-Ti magnetite *(4)*]. Angra dos Reis has two main ferromagnetic minerals with differing coercivities which were hypothesized to be low-Ti magnetite and kamacite or pyrrhotite *(4)*. In addition, the mean destructive field for an IRM of 2000 G for SAH 99555 is within the lower range of Angra dos Reis, but is most similar to D'Orbigny and a little higher than A-881371.

The S-ratio helps determine the identity of the major ferromagnetic minerals of the sample by showing the relative contributions of high-coercivity to low-coercivity minerals toward the magnetization of the sample. Notably, hematite has a high-coercivity while magnetite has a low-coercivity. The S-ratio ranges as classically from -1 to 1 per Thompson and Oldfield *(25)* and from 0 to 1 as per Bloemendal et. al. *(27)*. The S ratios of SAH 99555,5 are 0.97 and 0.99, respectively, as calculated by:

$$S_{classic} = -IRM_{-300mT}/IRM_{900mT}$$

$$S_{Bloemednal} = (1-IRM_{-300mT}/IRM_{900mT})/2$$

where IRM_{900mT} is assumed to be close to or greater than the saturation magnetization. These are very high S-ratios and show that the high-coercivity hematite is not an important factor in the magnetization of the sample. Combined with the information from the electron microprobe experiments, this provides further evidence that the proportion of hematite (due to terrestrial alteration) to magnetite is low. The primary magnetic mineral appears to be magnetite, which means that the high-coercivity component of the NRM is probably the result of a paleofield on the APB.

Paleointensity

Methods

After AF demagnetization, SAH 99555,5 underwent 4 AF paleointensity experiments. These were non-destructive, and therefore, only produce order of magnitude estimates on the paleofield that magnetized the angrite while on the APB. (This seems like a high uncertainty, but that is only by terrestrial standards where the questions being studied require much more accuracy. Here the potential source fields being tested for the angrites, as discussed in the introduction, vary in paleointensity by many orders of magnitude.)

Many different studies of terrestrial, extraterrestrial and synthetic samples have shown that the paleointensity of a given TRM is approximately proportional to the ratio of that thermoremanent NRM to the saturation IRM *(28-36)*. Further studies have shown that the ratio of the thermoremanent NRM to the ARM gained (also known as *f'*) is also roughly proportional to the NRM paleointensity *(37-42)*. The paleointensity estimate using this method will be closest to the actual value when the ARM bias field is close to the paleofield which produced the NRM *(43)*.

First, SAH 99555,5 was given an artificial ARM, acquired by increasing AF fields in constant DC bias fields of 0.5 G, 2 G, and 6 G. These AF fields were the same steps used for the AF demagnetization of the NRM up to 850 G. After these three sets of measurements, SAH 99555,5 was given a saturation IRM (with levels up to 8865 G) and then was AF demagnetized using the same steps as before.

Following the protocol described in Weiss et. al. (2008) *(4)* with a method based on that of Stephenson *(37)*, the NRM lost was plotted against the ARM gained for each of the three bias

fields to determine a paleointensity. NRM lost and ARM gained were computed by doing vector subtraction between the AF steps at increasing levels. Because SAH 99555,5 is in the pseudo single domain size range, the following formula and calibration factor were used to calculate the paleointensity estimate from the NRM/ARM ratio:

$$\text{ARM paleointensity } (\mu T) = (\Delta NRM/\Delta ARM)/1.34 \times (\text{bias field})$$

where ΔNRM and ΔARM are the vector-subtracted loss and gain, respectively, derived by performing a least squares fit to the paleointensity plot. This was done for each of the three bias fields used.

The fourth experiment plotted the NRM lost versus IRM lost following the methodology of Weiss et. al. (2008) *(4)* which essentially is the REM' method used by Gattacceca and Rochette *(36)* paired with the visualization style of Stephenson *(37)* to reduce the effect of noise. The IRM lost was similarly computed using vector subtraction between the AF steps at increasing levels. Since SAH 99555,5 has pseudo single domain grains, the following equation was used to determine the paleointensity:

$$\text{IRM paleointensity } (\mu T) = \Delta NRM/\Delta IRM \times 3000$$

where ΔNRM and ΔIRM are the vector-subtracted losses derived by performing a least squares fit to the paleointensity plot.

Results and Discussion

As noted before, the AF demagnetization of SAH 99555,5 showed that there were two components, a low-coercivity component and a high-coercivity component. However, from that set of data it is unclear where the "change" is, i.e. when the low-coercivity component

becomes unblocked. From the paleointensity plots of SAH 99555,5 (Fig. 18), it appears that there is a low-coercivity component with a steep slope and a high-coercivity component with a gentler slope. This change occurs between 85 G and 140 G. Therefore for the NRM v. ARM data, a least squares fit was done to the range from 140 G to 690 G (when the data starts getting noisy) to estimate the paleointensity (Table 6). For the NRM v. IRM data, the least squares fit was done from 130 G to 690 G as this gave a better R^2 value. Although between each step the change in moment due to the rotation should be minimal (i.e. not greatly affect the data), another least squares fit was also done from 290 G to 690 G, using the measurements made when the sample was not rotating. Due to the greater noise at these high levels and the shorter data range, these paleointensity estimates probably not accurate. This is shown by the larger confidence intervals as well as very low R^2 values. (A least squares fit for the low-coercivity component was done resulting in widely varied intensities from about 25 μT to 600 μT with large confidence intervals from 100 μT to 15 μT respectively. Clearly this is not a primary paleointensity.)

The ARM paleointensity estimates for the predicted high-coercivity component were 14.5 ± 2 μT (0.5 G bias field), 16.1 ± 0.6 μT (2 G bias field), and 15.7 ± 0.2 μT when the entire predicted range was used. The IRM paleointensity estimate was 8.0 ± 1 μT. These values are similar to those found for D'Orbigny and some of the samples of Angra dos Reis. Particularly, the plots look similar to those of D'Orbigny, with its well defined low coercivity component, and A-881371 as well (Fig. 19).

Conclusion

Electron microscopy studies show that SAH 99555 contains several ferromagnetic minerals including magnetite, titanomagnetite, and hematite. From these data alone, it is unclear how much these ferromagnetic minerals were affected by terrestrial alteration. However, using the S-ratio and the coercivity spectrum, it is clear that SAH 99555 contains one primary ferromagnetic mineral which in this case is magnetite. (The rest of the minerals are simply accessory ferromagnetic minerals.)

Although no specific change in direction of NRM is not seen, the data suggests that there is a low-coercivity component and a high-coercivity component of the NRM of SAH 99555,5, similar to D'Orbigny. The low-coercivity component is probably from a collector's hand magnet or the Earth's field. The paleointensity measurements of the high-coercivity component of SAH 99555,5 agree with the paleointensity estimates made for D'Orbigny and A-881371. Therefore, it appears that SAH 99555 does record a primary paleofield from when it was on the angrite parent body. This would be in fact the oldest known paleomagnetic record yet identified in a planetary rock.

Further studies should be done to test these conclusions. Specifically, additional AF demagnetization experiments would help in verifying the existence of the low-coercivity component of the paleofield. Thermomagnetic experiments could be used to determine the Curie point of the meteorite as well as show any magnetic transitions. This would help substantiate the claim that magnetite is the primary ferromagnetic mineral, and that the small amount of hematite in the SAH 99555 is not affecting the NRM. Finally, a fusion baked contact test should be performed on SAH 99555 for more confirmation that the paleofield measured

for SAH 99555,5 (i.e. the interior) is pre-terrestrial. This test takes mutually oriented AF measurements of the sample transversing the fusion crust to the interior. The exterior layer of the meteorite often is baked from entering the earth's atmosphere, and therefore has a different magnetization direction than the interior moment. The presence of an outer baked layer with NRM direction different than the interior or the Earth's field would indicate that any paleofield recorded by the interior is preterrestrial. If these tests all corroborate the conclusions presented in this paper, then SAH 99555,5 will be one more data point suggesting that the paleofield was generated internally on the APB *(4)*, and therefore that early planetesimal dynamos were present in the very early solar system.

References

1. Amelin Y. (2008) U-Pb ages of angrites, *Geochemica et Coscoshimica Act,* **72**, 221-232.
2. Amelin Y. (2008) The U Pb systematics of angrite Sahara 99555, *Geochimica Cosmochimica Acta* **72**, 4874-4885.
3. Baker J., Bizzarro M., Wittig N., Connelly J., and Haack H. (2005) Early planetesimal melting from an age of 4.5662Gyr for differentiated meteorites, *Nature* **436**, 7054, 1127-1131.
4. Weiss B.P., Berdahl J. S., Elkins-Tanton L., Stanley S., Lima E.A., and Carporzen L. (2008) Magnetism on the Angrite Parent Body and the Early Differentiation of Planetesimals, *Science* **322**, 713-716
5. Mittlefehldt D. W., Killgore M., and Lee M.T. (2002) Petrology and geochemistry of D'Orbigny, geochemistry of Sahara 99555, and the origin of angrites, *Meteoritics & Planetary Science* **37**, 3, 345-369.
6. Mittlefehldt D.W. and Lindstrom M.M. (1990) Geochemistry and genesis of the angrites, *Geochimica et Cosmochimica Acta* **54**, 3209-3218.
7. Sugiura N., Miyazaki A., and Yanai K. (2005) Widespread magmatic activities on the angrite parent body at 4562 Ma ago, *Earth Planets Space* **57**, e13-16.
8. Warren H. P. and Davis M.A. (1995) Consortium investigation of the Asuka-881371 angrite: Petrographic, electron microprobe, and ion microprobe observations, *Antarctic Meterorites XX*, NIPR, Tokyo, June 6-8, 1995, 257-260.
9. Mittlefehldt D.W. (2004). Achondrites, in: *Treatise on Geochemistry*, Holland H.D. and Turekian K.K. (Eds), Elsevier, Amsterdam. 291-324.
10. Kurat G., Varela M.E., Brandstatter F., Weckwerth G., Clayton R. N., Weber H.W., Schultz L., Wasch E., and Nazarov M.A. (2004) D'Orbigny: A non-igneous angritic achondrite?, *Geochimica et Cosmochimica Acta* **68**, 8, 1901-1921.
11. Butler R.F. (1998) *Paleomagnetism: Magnetic domains to geologic terranes*, University of Arizona, Tuscon, Arizona.
12. Connelly J.N., Bizarro M., Thrane K., and Baker J.A. (2008) The Pb-Pb age of Angrite SAH99555 revisited, *Geochimica et Cosmochimica Acta* **72**, 19, 4813-4824
13. Busemann H., Lorenzetti S., and Eugster O. (2006) Noble gases in D'Orbigny, Sahara 99555 and D'Orbigny glass—Evidence for early planetary processing on the angrite parent body, *Geochimica et Cosmochimica Acta* **70**, 5403-5425.
14. Bischoff A., Clayton R.N., Markl G., Mayeda T.K., Palme H., Schultz L., Srinivasan G., Weber H.W., Weckwerth G., and Wolf D. (2000) Mineralogy, Chemistry, Noble Gases, and Oxygen- and Magnesium-Isotopic Compositions of the Angrite Sahara 99555, *Meteoritics & Planetary Science*, **35**, Supplement, p.A27.
15. Mikouchi T., McKay G., Le L., and Mittlefehldt D.W. (2000) Preliminary Examination of Sahara 99555: Mineralogy and Experimental Studies of a New Angrite, *31st Annual Lunar and Planetary Science Conference*, March 13-17, 2000, Houston, Texas, 1970
16. Lyberatos A. (2007). Temperature dependence of the magnetization of titanomagnetites, *Journal of magnetism and Magnetic Materials*, **311**, 560-564.

17. Floss C., Crozaz G., McKay G, Mikouchi T., and Killgore M. (2003) Petrogenesis of angrites, *Geochimica et Cosmochimica Acta* **67**, 24, 4775-4789.
18. Crozaz G., Floss C., and Wadhwa M. (2003) Chemical alteration and REE mobilization in meteorites from hot and cold deserts, *Geochimica et Cosmochimica Acta* **67**, 24, 4727-4741.
19. Zhou W., Van der Voo R., Peacor D.R., Wang D., and Zhang Y. (2001) Low-temperature oxidation in MORB of titanomagnetite to titanomaghemite: A gradual process with implications for marine magnetic anomaly amplitudes, *Journal of Geophysical Research* **106**, B4, 6409-6421.
20. Garcia de Oliviera M.T., Formoso M.L.L., Indio da Costa Jr. M., and Meunier A.(2002) Titanomagnetite to titanomaghemite conversion in a weathered basalt profile from southern Paraná Basin, Brazil, *Clays and Clay Minerals* **50**, 4, 478-493.
21. Dunlop D.J. (2002) Theory and application of the Day plot (M_{rs}/M_s versus H_{cr}/H_c) 1. Theoretical curves and tests using titanomagnetite data, *Journal of Geophysical Research* **107**, B3, EPM 4-1, 2001JB000486.
22. Cisowski S. (1981) Interacting vs. non-interacting single domain behavior in natural and synthetic samples, *Physics of the Earth and Planetary Interiors* **26**, 56-62.
23. Lowrie W. and Fuller M. (1971) On the Alternating Field Demagnetization Characteristics of Multidomain Thermoremanent Magnetization in Magnetite, *Journal of Geophysical Research* **76**, 26, 6339-6349.
24. Xu S.and Dunlop D.J. (1995) Toward a better understanding of the Lowrie-Fuller test, *Journal of Geophysical Research* **100,** B11, 22533-22542.
25. Kruiver P. P. and Passier H. F. (2001) Coercivity analysis of magnetic phases in sapropel S1 related to variations in redox conditions, including an investigation of the S-ratio, *Geochemistry, Geophysics, and Geosystems* **2**, 2001GC000181.
26. Thomson R. and Oldfield F. (1986) *Environmental Magnetism*. Allen and Unwin, Concord, pp. 227
27. Bloemendal J., King J.W., Hall F.R. and Doh S.H. (1992) Rock magnetism of Late Neogene and Pleistocene deep-sea sediments: Relationship to sediment source, diagenetic processes and sediment lithology, *Journal of Geophysical Research* **97**, 4361–4375
28. Kohout T., Kletetschka G., Donadini F., Fuller M. and Herrero-Bervera E.(2008) Analysis of the natural remanent magnetization of rocks by measuring the efficiency ratio through alternating field demagnetization spectra, *Studia Geophysica et Geodaetica* **52**, 225-235.
29. Kletetschka G., Acuna M.H., Kohout T., Wasilewski P.J., and Connerney J.E.P. (2004) An Empirical Scaling Law for Acquisition of Thermoremanent Magnetization, *Earth and Planetary Science Letters* **226**, 521-528.
30. Kletetschka G., Kohout T., and Wasilewski P.J. (2003) Magnetic remanence in Murchison meteorite, *Meteoritics & Planetary Science* **38**, 399-406.
31. Fuller M., Cisowski S., Hart M., Haston R., Schmidke E. and Jarrard R. (1988), NRM:IRM(s) demagnetization plots; an aid to the interpretation of natural remanent magnetization, *Geophyical Research Letters* **15**, 518–521.
32. Fuller M. and Cisowski S. M. (1987), in *Geomagnetism,* J. A. Jacobs, Ed., Academic Press, Orlando, vol. 2, 307-455.

33. Fuller M., Kidane T. and Ali J. (2002) AF demagnetization characteristics of NRM, compared with anhysteretic and saturation isothermal remanence: an aid in the intrepretation of NRM, *Physics and Chemistry of the Earth* **27**,1169–1177.
34. Kletetschka G., Fuller M.D., Kohout T., Wasilewski P.J., Herrero-Bervera E., Ness N.F. and Acuna M.H. (2006) TRM in low magnetic fields: a minimum field that can be recorded by large multidomain grains, *Physics of the Earth and Planetary Interiors,* **154**, 290–298.
35. Verrier V. and Rochette P. (2002) Estimating peak currents at ground lightning impacts using remanent magnetization, *Geophysical Research Letters* **29,** 1867.
36. Gattacceca J. and Rochette P. (2004) Toward a robust normalized magnetic paleointensity method applied to meteorites, *Earth Planetary Science Letters* **227**, 377-393.
37. Stephenson A., Collinson D. W., and Runcorn S. K.(1974) Lunar magnetic field palaeointensity determinations on Apollo 11, 16, and 17 rocks, *Proceedings Tenth Lunar Planetary Science Conference*, 2859-2871.
38. Stephenson A., Runcorn S. K., Collinson D. W., (1977) Paleointensity estimates from lunar samples 10017 and 10020, *Proceedings Lunar Planetary Science Conference 8th*, 679.-687
39. Hoffman K.A., Baker J.R. and Banerjee S.K. (1979) Combining paleointensity methods; a dual-valued determination on lunar sample 10017,135, *Physics of the Earth and Planetary Interiors* **20**, 317–323.
40. Carmichael C. M. (1977), Paleointensity studies of oceanic basalts from DSDP Leg 37 and NRM/ARM ratios of oceanic and recent lavas, *Physics of the Earth and Planetary Interiors* **13**, 332-338.
41. Sugiura N. and Strangway D.W. (1983) Magnetic paleointensity determination on lunar sample 62235, *Journal of Geophysical Research* **88**, A684–A690
42. Morden S.J. (1992) A magnetic study of the Millbillillie (eucrite) achondrite: Evidence for a dynamo-type magnetising field, *Meteoritics* **27**,560–576.
43. Bailey M.E. and Dunlop D.J.(1977), On the use of anhysteretic remanent magnetization in paleointensity determination, *Physics of the Earth and Planetary Interiors* **13,** 360–362.
44. Tauxe L., and Yamazaki T. (2007) Paleointensities, in *Treatise on Geophysics,* vol.5, *Geomagnetism,* 509-563.

References alphabetically

Amelin Y. (2008) U-Pb ages of angrites, *Geochemica et Coscoshimica Act,* **72**, 221-232.

Amelin Y. (2008) The U Pb systematics of angrite Sahara 99555, *Geochimica Cosmochimica Acta* **72**, 4874-4885.

Bailey M.E. and Dunlop D.J.(1977), On the use of anhysteretic remanent magnetization in paleointensity determination, *Physics of the Earth and Planetary Interiors* **13,** 360–362.

Baker J., Bizzarro M., Wittig N., Connelly J., and Haack H. (2005) Early planetesimal melting from an age of 4.5662Gyr for differentiated meteorites, *Nature* **436**, 7054, 1127-1131.

Bischoff A., Clayton R.N., Markl G., Mayeda T.K., Palme H., Schultz L., Srinivasan G., Weber H.W., Weckwerth G., and Wolf D. (2000) Mineralogy, Chemistry, Noble Gases, and Oxygen- and Magnesium-Isotopic Compositions of the Angrite Sahara 99555, *Meteoritics & Planetary Science*, **35**, Supplement, p.A27.

Bloemendal J., King J.W., Hall F.R. and Doh S.H. (1992) Rock magnetism of Late Neogene and Pleistocene deep-sea sediments: Relationship to sediment source, diagenetic processes and sediment lithology, *Journal of Geophysical Research* **97**, 4361–4375

Busemann H., Lorenzetti S., and Eugster O. (2006) Noble gases in D'Orbigny, Sahara 99555 and D'Orbigny glass—Evidence for early planetary processing on the angrite parent body, *Geochimica et Cosmochimica Acta* **70**, 5403-5425.

Butler R.F. (1998) *Paleomagnetism: Magnetic domains to geologic terranes*, University of Arizona, Tuscon, Arizona.

Carmichael C. M. (1977), Paleointensity studies of oceanic basalts from DSDP Leg 37 and NRM/ARM ratios of oceanic and recent lavas, *Physics of the Earth and Planetary Interiors* **13**, 332-338.

Cisowski S. (1981) Interacting vs. non-interacting single domain behavior in natural and synthetic samples, *Physics of the Earth and Planetary Interiors* **26**, 56-62.

Connelly J.N., Bizarro M., Thrane K., and Baker J.A. (2008) The Pb-Pb age of Angrite SAH99555 revisited, *Geochimica et Cosmochimica Acta* **72**, 19, 4813-4824

Crozaz G., Floss C., and Wadhwa M. (2003) Chemical alteration and REE mobilization in meteorites from hot and cold deserts, *Geochimica et Cosmochimica Acta* **67**, 24, 4727-4741.

Dunlop D.J. (2002) Theory and application of the Day plot (M_{rs}/M_s versus H_{cr}/H_c) 1. Theoretical curves and tests using titanomagnetite data, *Journal of Geophysical Research* **107**, B3, EPM 4-1, 2001JB000486.

Floss C., Crozaz G., McKay G, Mikouchi T., and Killgore M. (2003) Petrogenesis of angrites, *Geochimica et Cosmochimica Acta* **67**, 24, 4775-4789.

Fuller M. and Cisowski S. M. (1987), in *Geomagnetism,* J. A. Jacobs, Ed., Academic Press, Orlando, vol. 2, 307-455.

Fuller M., Cisowski S., Hart M., Haston R., Schmidke E. and Jarrard R. (1988), NRM:IRM(s) demagnetization plots; an aid to the interpretation of natural remanent magnetization, *Geophyical Research Letters* **15**, 518–521.

Fuller M., Kidane T. and Ali J. (2002) AF demagnetization characteristics of NRM, compared with anhysteretic and saturation isothermal remanence: an aid in the intrepretation of NRM, *Physics and Chemistry of the Earth* **27**,1169–1177.

Garcia de Oliviera M.T., Formoso M.L.L., Indio da Costa Jr. M., and Meunier A.(2002) Titanomagnetite to titanomaghemite conversion in a weathered basalt profile from southern Paraná Basin, Brazil, *Clays and Clay Minerals* **50**, 4, 478-493.

Gattacceca J. and Rochette P. (2004) Toward a robust normalized magnetic paleointensity method applied to meteorites, *Earth Planetary Science Letters* **227**, 377-393.

Hoffman K.A., Baker J.R. and Banerjee S.K. (1979) Combining paleointensity methods; a dual-valued determination on lunar sample 10017,135, *Physics of the Earth and Planetary Interiors* **20**, 317–323.

Kletetschka G., Kohout T., and Wasilewski P.J. (2003) Magnetic remanence in Murchison meteorite, *Meteoritics & Planetary Science* **38**, 399-406.

Kletetschka G., Acuna M.H., Kohout T., Wasilewski P.J., and Connerney J.E.P. (2004) An Empirical Scaling Law for Acquisition of Thermoremanent Magnetization, *Earth and Planetary Science Letters* **226**, 521-528.

Kletetschka G., Fuller M.D., Kohout T., Wasilewski P.J., Herrero-Bervera E., Ness N.F. and Acuna M.H. (2006) TRM in low magnetic fields: a minimum field that can be recorded by large multidomain grains, *Physics of the Earth and Planetary Interiors,* **154**, 290–298.

Kohout T., Kletetschka G., Donadini F., Fuller M. and Herrero-Bervera E.(2008) Analysis of the natural remanent magnetization of rocks by measuring the efficiency ratio through alternating field demagnetization spectra, *Studia Geophysica et Geodaetica* **52**, 225-235.

Kruiver P. P. and Passier H. F. (2001) Coercivity analysis of magnetic phases in sapropel S1 related to variations in redox conditions, including an investigation of the S-ratio, *Geochemistry, Geophysics, and Geosystems* **2**, 2001GC000181.

Kurat G., Varela M.E., Brandstatter F., Weckwerth G., Clayton R. N., Weber H.W., Schultz L., Wasch E., and Nazarov M.A. (2004) D'Orbigny: A non-igneous angritic achondrite?, *Geochimica et Cosmochimica Acta* **68**, 8, 1901-1921.

Lowrie W. and Fuller M. (1971) On the Alternating Field Demagnetization Characteristics of Multidomain Thermoremanent Magnetization in Magnetite, *Journal of Geophysical Research* **76**, 26, 6339-6349.

Lyberatos A. (2007). Temperature dependence of the magnetization of titanomagnetites, *Journal of magnetism and Magnetic Materials*, **311**, 560-564.

Mikouchi T., McKay G., Le L., and Mittlefehldt D.W. (2000) Preliminary Examination of Sahara 99555: Mineralogy and Experimental Studies of a New Angrite, *31st Annual Lunar and Planetary Science Conference*, March 13-17, 2000, Houston, Texas, 1970

Mittlefehldt D.W. and Lindstrom M.M. (1990) Geochemistry and genesis of the angrites, *Geochimica et Cosmochimica Acta* **54**, 3209-3218.

Mittlefehldt D. W., Killgore M., and Lee M.T. (2002) Petrology and geochemistry of D'Orbigny, geochemistry of Sahara 99555, and the origin of angrites, *Meteoritics & Planetary Science* **37**, 3, 345-369.

Mittlefehldt D.W. (2004). Achondrites, in: *Treatise on Geochemistry*, Holland H.D. and Turekian K.K. (Eds), Elsevier, Amsterdam. 291-324.

Morden S.J. (1992) A magnetic study of the Millbillillie (eucrite) achondrite: Evidence for a dynamo-type magnetising field, *Meteoritics* **27**,560–576.

Stephenson A., Collinson D. W., and Runcorn S. K.(1974) Lunar magnetic field palaeointensity determinations on Apollo 11, 16, and 17 rocks, *Proceedings Tenth Lunar Planetary Science Conference*, 2859-2871.

Stephenson A., Runcorn S. K., Collinson D. W., (1977) Paleointensity estimates from lunar samples 10017 and 10020, *Proceedings Lunar Planetary Science Conference 8th*, 679.-687

Sugiura N. and Strangway D.W. (1983) Magnetic paleointensity determination on lunar sample 62235, *Journal of Geophysical Research* **88**, A684–A690

Sugiura N., Miyazaki A., and Yanai K. (2005) Widespread magmatic activities on the angrite parent body at 4562 Ma ago, *Earth Planets Space* **57**, e13-16.

Tauxe L., and Yamazaki T. (2007) Paleointensities, in *Treatise on Geophysics,* vol.5, *Geomagnetism,* 509-563.

Thomson R. and Oldfield F. (1986) *Environmental Magnetism*. Allen and Unwin, Concord, pp. 227

Verrier V. and Rochette P. (2002) Estimating peak currents at ground lightning impacts using remanent magnetization, *Geophysical Research Letters* **29,** 1867.

Warren H. P. and Davis M.A. (1995) Consortium investigation of the Asuka-881371 angrite: Petrographic, electron microprobe, and ion microprobe observations, *Antarctic Meterorites XX*, NIPR, Tokyo, June 6-8, 1995, 257-260.

Weiss B.P., Berdahl J. S., Elkins-Tanton L., Stanley S., Lima E.A., and Carporzen L. (2008) Magnetism on the Angrite Parent Body and the Early Differentiation of Planetesimals, *Science* **322**, 713-716

Xu S.and Dunlop D.J. (1995) Toward a better understanding of the Lowrie-Fuller test, *Journal of Geophysical Research* **100,** B11, 22533-22542.

Zhou W., Van der Voo R., Peacor D.R., Wang D., and Zhang Y. (2001) Low-temperature oxidation in MORB of titanomagnetite to titanomaghemite: A gradual process with implications for marine magnetic anomaly amplitudes, *Journal of Geophysical Research* **106**, B4, 6409-6421.

Table Appendix

Table 1: Data on Petrology from Electron Microscopy

Label	El%					Atomic %				
	Fe	Ti	Al	O	Total	Fe	Ti	Al	O	CatTot
1	53.85	16.05	0.8686	28.16	98.93	31.19	10.836	1.0413	56.933	100
2	55.25	13.37	1.4182	27.88	97.92	32.295	9.114	1.7157	56.876	100
3	53.29	16.22	1.1825	28.55	99.24	30.575	10.85	1.4043	57.17	100
4	52.88	16.87	0.9304	28.39	99.06	30.469	11.332	1.1096	57.09	100
5	52.6	16.09	1.2032	28.7	98.6	30.225	10.782	1.4311	57.561	100
AVG	53.574	15.72	1.12058	28.336	98.75	30.9508	10.5828	1.3404	57.126	100
1'	55.57	8.91	2.9276	27.78	95.18	32.882	6.145	3.586	57.387	100
2'	56.87	7.3	2.6799	28.7	95.55	33.234	4.977	3.242	58.547	100
A	69.61	0.5112	0.5036	26.79	97.42	42.255	0.3617	0.6326	56.751	100
B	68.87	0.0521	0.0768	27.63	96.63	41.607	0.0367	0.096	58.26	100
C	69.67	0.1978	0.2704	27.87	98	41.536	0.1375	0.3337	57.993	100

Representative data from quantitative wavelength dispersive spectroscopy on the electron microprobe to determine the chemistry of particular ferromagnetic grains in SAH 99555,5. Grains 1-5 are all crystals of the large, relatively common iron-titanium oxide in the crystal. These data points are then averaged to find a general composition for this mineral, displayed by the row labeled AVG. Grains 1' and 2' are the iron-titanium oxide found around the rims of the troilite. Grains A-C are the grains found which contained very little to no Ti or Al (as seen above). The first column gives the grain label; the second through fifth give the respective elemental % of the 4 elements tested for; the sixth column gives the total percentage of elements in the mineral represented by the 4 tested; the seventh through tenth columns give normalized atomic proportions from the data measured by the microprobe, the 11th column gives the cation total to show the accuracy of the normalization.

Table 2: Calculations to Find General Chemical Formula

Step 1: Spread oxygen around from Atomic %					
Label	**FeO**	**TiO_2**	**Al_2O_3**	**Fe_2O_3**	**O**
1	26.1719	21.672	1.56195	7.52715	0.000E+00
2	24.7361	18.228	2.57355	11.33835	0.000E+00
3	24.9979	21.7	2.10645	8.36565	0.000E+00
4	25.8838	22.664	1.6644	6.8778	0.000E+00
5	22.9743	21.564	2.14665	10.87605	0.000E+00
AVG	24.9528	21.1656	2.0106	8.997	0.000E+00
1'	19.21	12.29	5.379	20.508	0.000E+00
2'	12.242	9.954	4.863	31.488	0.000E+00
A	16.6076	0.7234	0.9489	38.4711	0.000E+00
B	8.7358	0.0734	0.144	49.3068	0.000E+00
C	10.1731	0.275	0.50055	47.04435	0.000E+00
Step 2: Correct Atomic Percentages					
Label	**Fe^{+2}**	**Fe^{+3}**	**Ti**	**Al**	**O**
1	26.1719	5.0181	10.836	1.0413	56.933
2	24.7361	7.5589	9.114	1.7157	56.876
3	24.9979	5.5771	10.85	1.4043	57.17
4	25.8838	4.5852	11.332	1.1096	57.09
5	22.9743	7.2507	10.782	1.4311	57.561
AVG	24.9528	5.998	10.5828	1.3404	57.126
1'	19.21	13.672	6.145	3.586	57.387
2'	12.242	20.992	4.977	3.242	58.547
A	16.6076	25.6474	0.3617	0.6326	56.751
B	8.7358	32.8712	0.0367	0.096	58.26
C	10.1731	31.3629	0.1375	0.3337	57.993
Step 3: Find Weight Percentages (plot on ternary diagram)					
Label	**%FeO**	**%Fe_2O_3**	**%TiO_2**	**%Al_2O_3**	
1	0.607698	0.116518	0.25160621	0.024178	
2	0.573595	0.17528	0.2113406	0.039785	
3	0.583664	0.130217	0.25333125	0.032788	
4	0.603203	0.106855	0.26408393	0.025858	
5	0.54136	0.170854	0.25406415	0.033722	
AVG	0.582003	0.139898	0.24683491	0.031264	

1'	0.450801	0.3208411	0.14420482	0.084153
2'	0.295322	0.5064048	0.12006369	0.078209
A	0.383997	0.5930131	0.00836314	0.014627
B	0.209292	0.7875284	0.00087926	0.0023
C	0.242175	0.7466077	0.00327325	0.007944

Step 4: Find Formula					
Label	**Fe^{+2}**	**Fe^{+3}**	**Ti**	**Al**	**O**
AVG	1.747211	0.419984	0.7410146	0.093856	4
1'	1.338979	0.9529684	0.42832	0.249952	4
2'	0.836388	1.4341982	0.3400345	0.221497	4
A	1.170559	1.8077144	0.02549382	0.044588	4
B	0.59978	2.2568623	0.00251974	0.006591	4
C	0.701678	2.1632197	0.0094839	0.023017	4

The table shows the steps of the calculations performed to find the general formula for each of the ferromagnetic minerals as well as the relative abundance of ferric v. ferrous iron and the weight percentage of oxides (used for the ternary diagram). In Step 1, the atomic % was used and the oxygen atoms were distributed among the cations to form oxides (with correct bonding). Step 2 took this data and converted it back into atomic proportions, but now had distinct ferric v. ferrous iron. From this data, the weight percentages were calculated (Step 3). This data could be plotted on a ternary diagram in order to narrow down whether the mineral should be O_4 or O_3 as well as provide visualization of the chemistry. Step 4 found the general chemical formula by using the atomic percentages and forcing there to be 4 oxygen. For the large, abundant ferromagnetic mineral (high-Ti titanomagnetite), the average of the 5 sampled grains was used.

Table 3: Summary of Hysteresis Data

Meteorite	Sample	Mass (mg)	X_p ($\times 10^{-5}$ Am^2T^{-1})	M_{rs} ($\times 10^{-5}$ Am^2)	M_s ($\times 10^{-7}$ Am^2)	H_c (mT)	M_{rs}/M_s	H_{cr}/H_c
SAH 99555	,5c	19	0.88	32.2	16.2	17.5	0.20	1.72
D'Orbigny*	11	51	1.8	58	20.9	17.5	0.27	1.55
	12	24	0.69	26.1	10	18	0.26	1.51
A-881371*	,63	66	1.9	34.1	16.2	16.3	0.21	1.72
Angra dos Reis*	M2	90†	0.19	7.58	8.29	13.5	0.09	2.65
	3S1	20	0.26	2.28	3.01	15	0.08	6.42

This data is from the VSM experiment at room temperature which plotted a hysteresis loop. The first column gives the meteorite name; the second column gives the name of the subsample; the third column gives the sample mass; the fourth column gives the paramagnetic susceptibility as estimated from the high-field slope of the hysteresis data; the fifth column gives the saturation remanent moment; the sixth column gives the saturation moment; the seventh column gives the coercivity; the eighth column gives the computed squareness which is the ratio of saturation remanent magnetization to saturation magnetization; the ninth column gives the ratio of coercivity of remanence (from IRM experiments, Table 4) to coercivity.

*The data on these meteorites is from Weiss et. al. (2008) *(4)*.

†Mass listed for this subsample is approximate because it was only weighed after thermomagnetic experiments were performed on it. It is within a factor of 2 of actual mass.

Table 4: GRM Measurements

Type	Level	Declination	Inclination	Moment (G)
AF	15	209.8	31.2	4.50E-05
UAF	15	205.8	30.9	4.52E-05
AF	100	201	26.6	5.34E-06
UAF	100	202.6	28.1	5.06E-06
AF	200	216.7	-1.8	1.85E-06
UAF	200	219.7	14.4	1.65E-06
AF	300	272.7	12.4	1.74E-06
UAF	300	250.1	19	8.72E-07
AF	400	291.6	-2.3	1.75E-06
UAF	400	286.4	-10.8	5.66E-07
AF	500	322.2	35.4	1.20E-06
UAF	500	289.5	-5.4	1.14E-06
AF	600	279.1	-2.1	1.47E-06
UAF	600	268	25.9	1.53E-06
AF	700	277.3	-19.2	2.00E-06
UAF	700	280.6	-21.9	1.93E-06
AF	800	270.6	14.3	1.72E-06
UAF	800	295	-1.4	7.18E-07
AF	850	267.1	49.4	1.12E-06
UAF	850	281.8	43.2	1.05E-06

GRM tests (uniaxial AF measurements) after the vector summation of the three components are compared with the normal NRM measurement at the same AF level. The first column gives the type of measurement; the second column gives the AF level in G; the third and fourth columns give the declination and inclination in degrees; the fifth column gives the measured moment in G.

Table 5: Summary of Rock Magnetic Data

Meteorite	Sample	S ratio	R	MDF ARM (mT)	MDF IRM (mT)	L-F Test	Hcr (mT)
SAH 99555	,5	0.97	0.31	17.3	19.6	H	30.1
D'Orbigny*	11	0.95	0.33	15.3	18.2	H	27.2
	12	0.96	0.32	15.9	18.1	L/H	27.2
	F1	0.96	0.32	16.2	19.1	H	29.3
	F2	0.95	0.27	18	18.3	L/H	35.9
	F6	0.97	0.3	15.4	16.4	H	27.3
	FB8	0.95	0.31	16.1	18	L/H	27.8
	FB10AA	0.96	0.32	13.6	15.8	H	24.7
	FB10AB	0.95	0.31	17.3	18.2	L/H	28.9
	FB10B	0.96	0.32	15.3	18	H	28
	FB14	0.96	0.31	15	15.9	H	25.7
A-881371*	,63	0.97	0.3	15.1	17.1	H	27.9
Angra dos Reis*	M3	0.38	0.4	17.6	40.6	L	73.4
	M4	0.4	0.42	16.4	29.6	L	52.5
	M6	0.47	0.39	18.9	30	L	58.6
	M7	0.33	0.4	18.4	51.7	L/H	94
	3S1	0.34	0.39	15.2	52.6	L/H	96.3
	AMC3	0.78	0.31	18.6	20.4	L	31.9
	AMC16	0.82	0.32	18	19.2	L	27.8

This data is from the ARM and IRM studies on the sample performed at room temperature and measured on the 2G Superconducting Rock Magnetometer. The first column gives the meteorite name; the second the subsample name, the third the S-ratio = $-IRM_{-300mT}/IRM_{900mT}$ from *(25)*; the fourth column gives the Cisowski R value *(21)*; the fifth column gives the mean destructive field for an ARM acquired in a 2000 G peak AF field with a DC bias field of 20 G; the sixth column similarly gives the mean destructive field for an IRM_{200mT}; the seventh column gives the outcome of the Lowrie-Fuller test *(22 ,23)* where L means low-field type with more stable ARM, H means high-field type with more stable IRM, and L/H means ARM and IRM are equally stable; the eight column gives the coercivity of remanence. All the masses of the samples studied here are listed in Table 6 (except D'Orbigny FB10AB which has a mass of 2.1 mg)

*Data on these meteorites from Weiss, et. al. (2008) *(4)*

Table 6: Summary of Paleointensity Estimates

Meteorite	Sample	Source	Mass (mg)	ARM Paleointensity			IRM Paleointensity (μT)
				50 μT bias	200 μT bias	600 μT bias	
SAH 99555	,5		132	14.5±2†	16.1±0.6†	15.7±0.2†	8.0±1†
				2.4±5	2.4±2	2.6±0.6	1.4±1
D'Orbigny*	F1	PS	75	12±3	15±3	13±3	9.6±2
	F2	PS	10	10±5	18±4	17±4	15±3
	F6	MT	75	9.2±4	11±3	10±2	7.7±2
	11	MT	51	14±10	20±7	12±4	17±5
	12	MT	24	17±15**	17±21**	26±23**	21±18
	FB8	MT	22	26±12	24±5	25±5	21±5
	FB10AA	MT	28	7.2±18	18±15	20±17	16±14
	FB10B	MT	21	29±18	26±17	22±16	20±14
	FB14	MT	163	8.8±3	13±4	14±4	12±4
A-881371*	,63	NIPR	66	8.1‡	6.9‡	7.1‡	2.2‡
Angra dos Reis*	M3	MNB	20	7.2±6	6.9±5	7.1±5	7.8±5
	M4	MNB	7	16±9	13±6	13±6	22±8
	M6	MNB	40	12‡	11‡	11‡	5.1‡
	M7	MNB	70	36±5	28±2	28±2	35±3
	3S1	MNB	20	2.8±9**	41±23**	31±23**	16±14
	AMC3	AMNH	58	20±0.9	17±0.7	15±0.5	21±1.2
	AMC16	AMNH	76	17±0.9	16±0.4	15±0.3	22±0.5

This data is the paleointensity estimates for the high-coercivity components of the listed meteorites. The first column gives the name of the meteorite; the second column gives the subsample name; the third column gives the source of the sample (PS = private source, MT = La Memoire de la Terre, NIPR = National Institute of Polar Research, Japan, MNB = Museu Nacional, Brasil, AMNH = American Museum of National History); the fourth column gives the mass of the sample; the fifth through seventh columns give the paleointensity estimate in microteslas found using the ARM method [Paleointensity = (NRM/ARM)/1.34 × (bias field in microteslas) following the method for pseudo single domain grains (*4, 36*)] with each column denoting a different bias field; and the final column gives the paleointensity estimate in microteslas found using the IRM method (Paleointensity = NRM/IRM x 3000) (*4, 35*). The uncertainties given are formal 95% confidence intervals from the least squares fitting to the paleointensity plots. The actual uncertainty for each value is estimated to be larger by a factor of ~3 because of the poorly understood proportionality of the ratio of IRM and ARM to TRM.

* The data for these meteorites is from Weiss, et. al. (2008) *(4)*

†The NRM data for SAH99555,5 contains small errors for the measurements below 280 G due to the rotation of the sample within the magnetometer. However, AF demagnetization as well as the paleointensity plots suggests that there is a low-coercivity and a high-coercivity component to the NRM. The first row gives the paleointensity estimate for steps of 140 G to 690 G (for ARM) and 130 G to 690 G (for IRM). This is where the high-coercivity component appears to begin and where the least squares fit was best. The error in the NRM data is very small per step and shouldn't greatly affect the estimation method. The second row gives the paleoestimates made using the steps of 290 G to 690 G. However, due to more noise at high AF levels as well as a shorter range, the latter set has higher uncertainties and is probably less accurate than the first row.

**The ARM paleointensities for these two samples were measured after the saturation IRM Experiments which is why they have such high uncertainties.

‡ These samples had a great deal of noise at high AF values which caused a poor least squares fit. Therefore the paleointensity estimates listed here were calculated by taking the ratio of the NRM remaining after removal of the low-coercivity component to the ARM or IRM after removal of the low-coercivity component. This is why it lacks confidence intervals as opposed to the other least squares fit estimates.

Figure Appendix

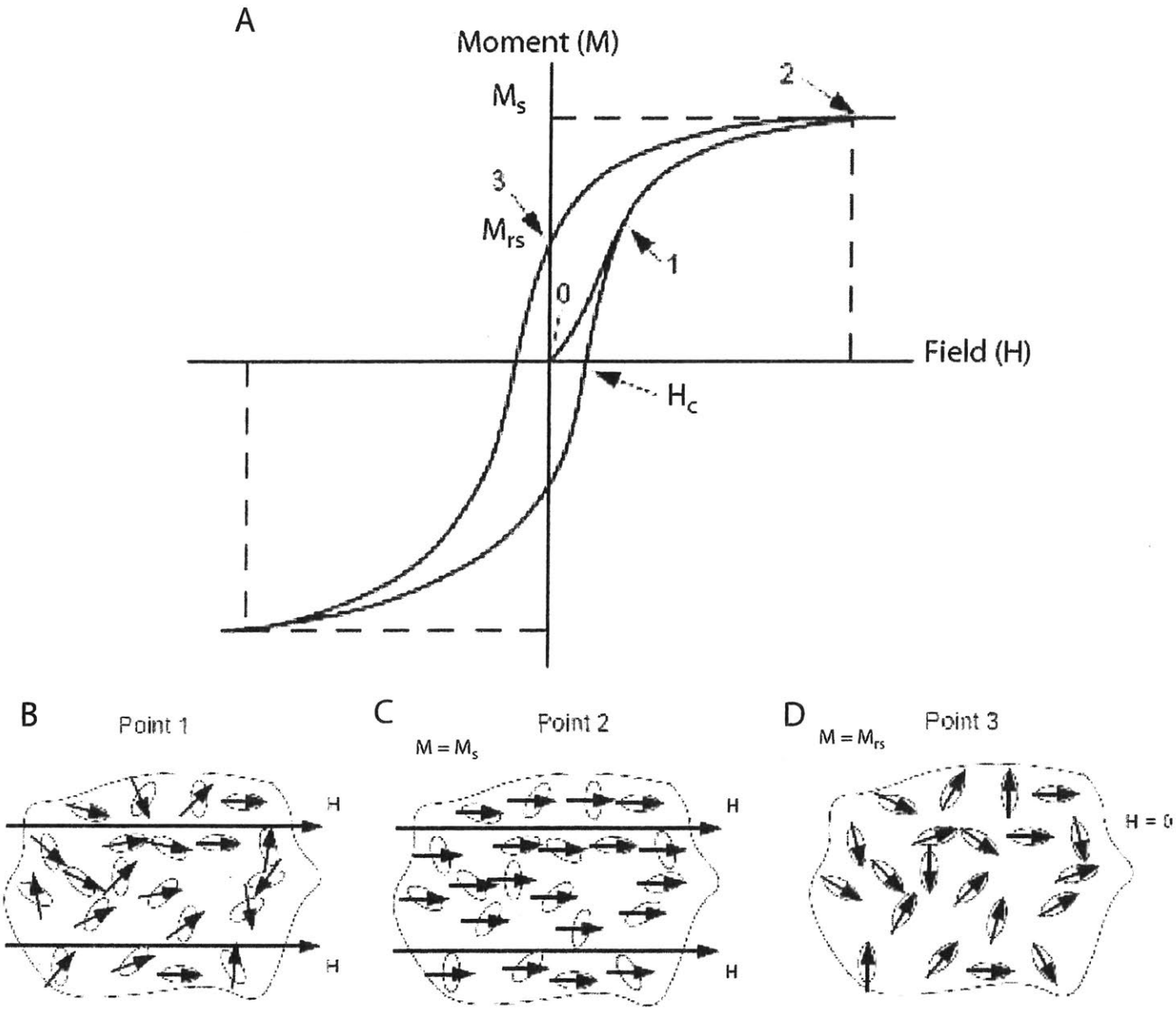

Figure 1: Theoretical hysteresis loop for rock with elongated SD grains. (A) shows the hysteresis loop with associated important values while (B), (C), and (D) detail the magnetization in the rock at particular points along the loop. (B) is when the applied field is slowly increasing in strength. At point 2 (C), the rock has reached the saturation magnetization (where M_s = saturation moment) and all the moments of the SD grains point in the direction of the applied field. At point 3 (D), the applied field has decreased again slowly down to zero. The moments of the individual SD grains snap to the elongated axis. The total moment of the rock when the applied field is zero is the saturation remanent moment (M_{rs}.) Figures modified from *(17)*.

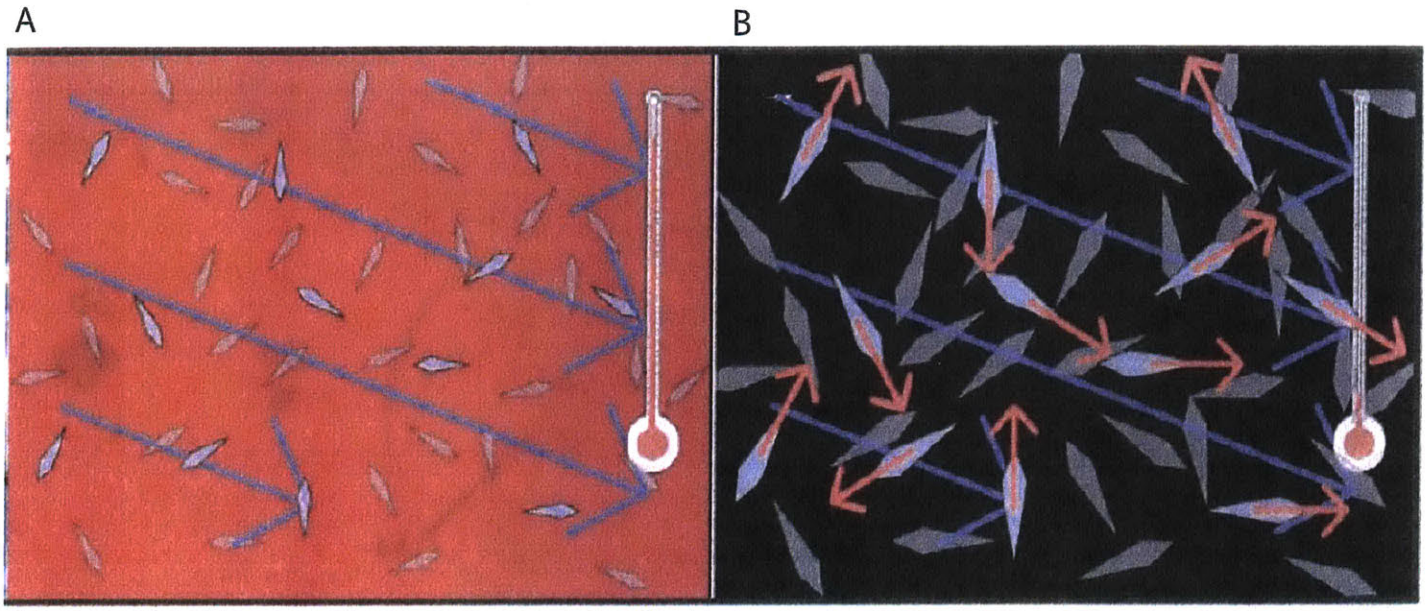

Figure 1: TRM theory. (A) is when the rock is above the Curie temperature. The direction of the applied field is shown with blue arrows, and the newly-formed crystals which later become magnetic are light blue. (B) is when the rock is below the Curie temperature but above the blocking temperature. The direction of the applied field is shown by the blue arrows. The light blue minerals are now ferromagnetic and the moments of these elongated grains are the red arrows. Figure modified from *(43)*.

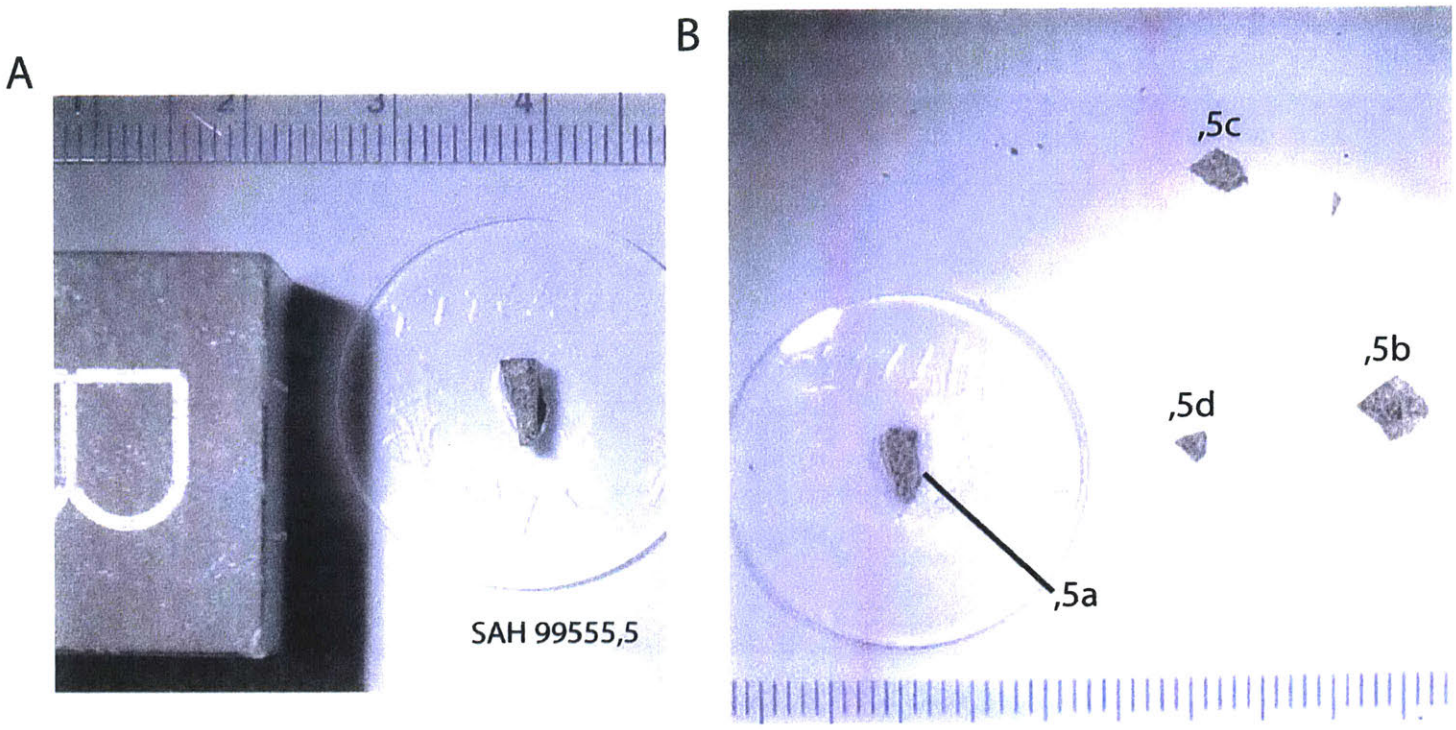

Figure 3: Photographs of breaking of SAH 99555,5. Direction of sample shown by black 1 inch cube. The clear ruler is a mm scale. (A) shows SAH 99555,5 mounted on a quartz disk for use in the 2G magnetometer. (B) shows the resulting 4 subsamples (plus dust) after SAH 99555,5 was broken. SAH 99555,5 weighed 132 mg. SAH 99555,5b is 55 mg, subsample ,5c is 19 mg, and subsample ,5d is 4.1 mg.

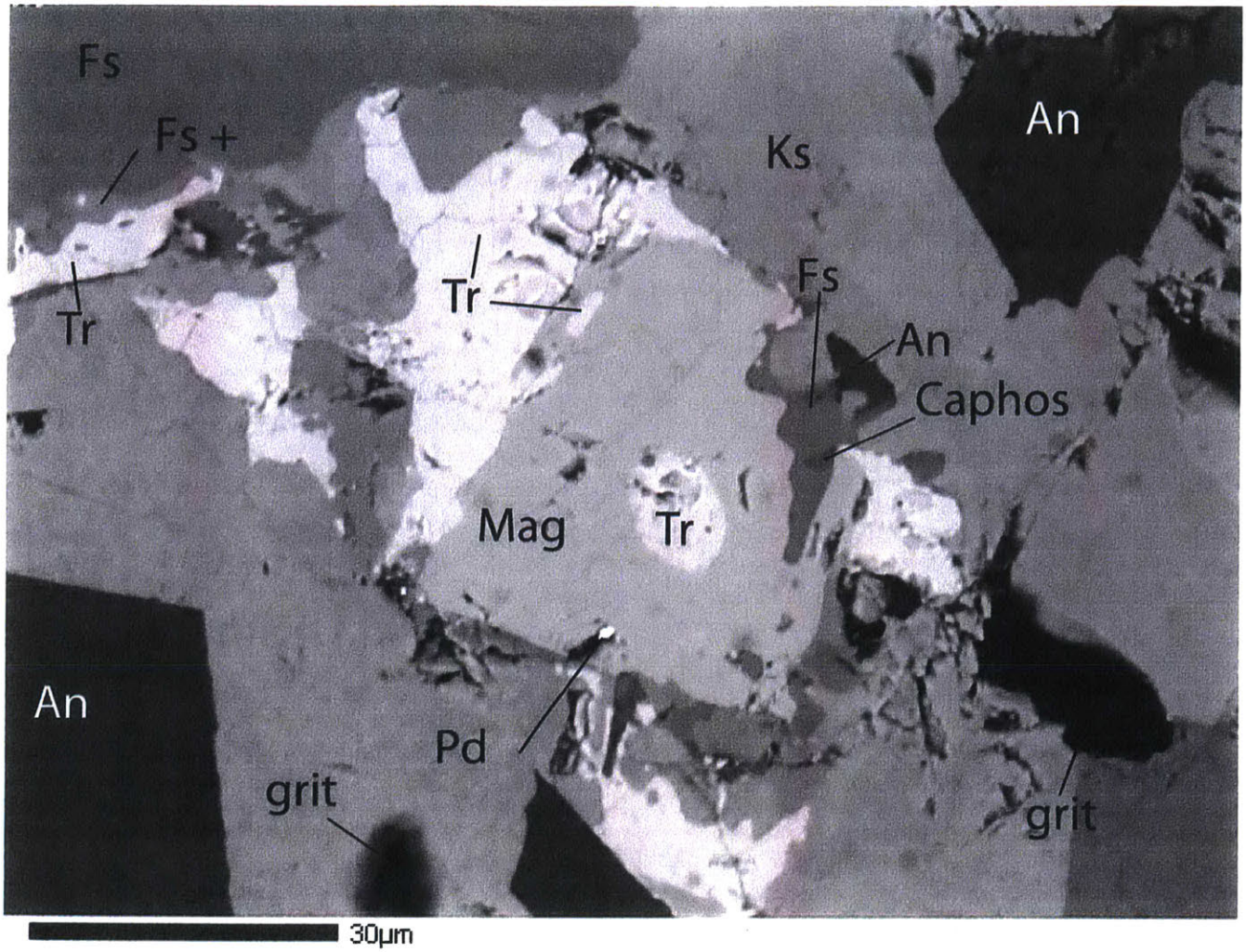

Figure 4: Backscatter electron microscopy imaging of SAH 99555,5b showing basic mineralogy. Ks = kirschsteinite, Fs = fassaitic clinopyroxene, Fs+ = fassaitic clinopyroxene with an increased % of Fe, An = anorthite, Tr = troilite, Caphos = calcium phosphate, Mag = ferromagnetic mineral identified as high-Ti titanomagnetite with formula $Fe_{2.26}Ti_{0.74}O_4$, Pd = paladium, grit = poorly polished section with remnants of grit from the polishing paper

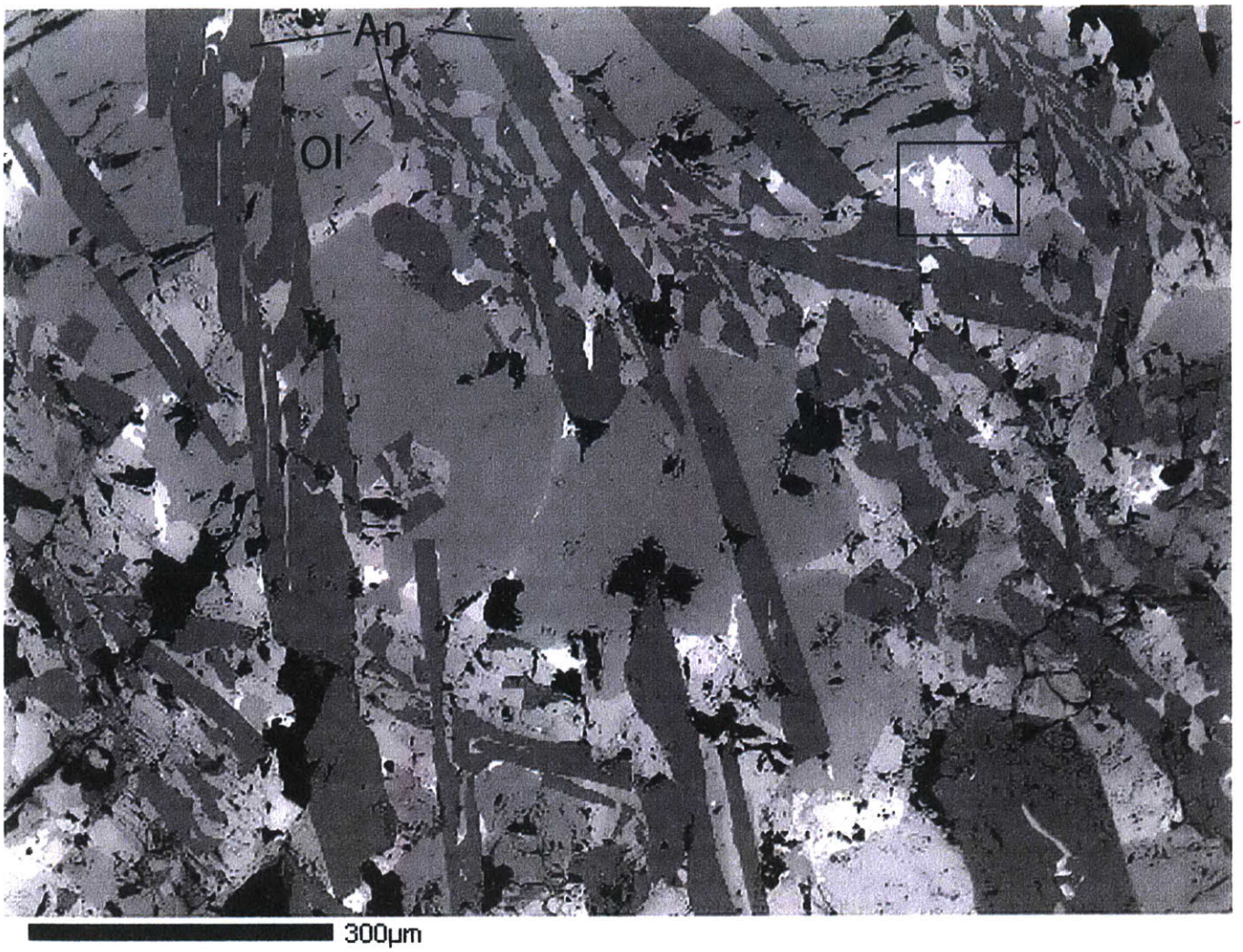

Figure 5: Backscatter electron microscopy imaging of SAH 99555,5b showing the complex intergrowth pattern between anorthite and olivine. Ol = olivine (often kirschsteinite), An = anorthite. Box around the area shown in Figure 4.

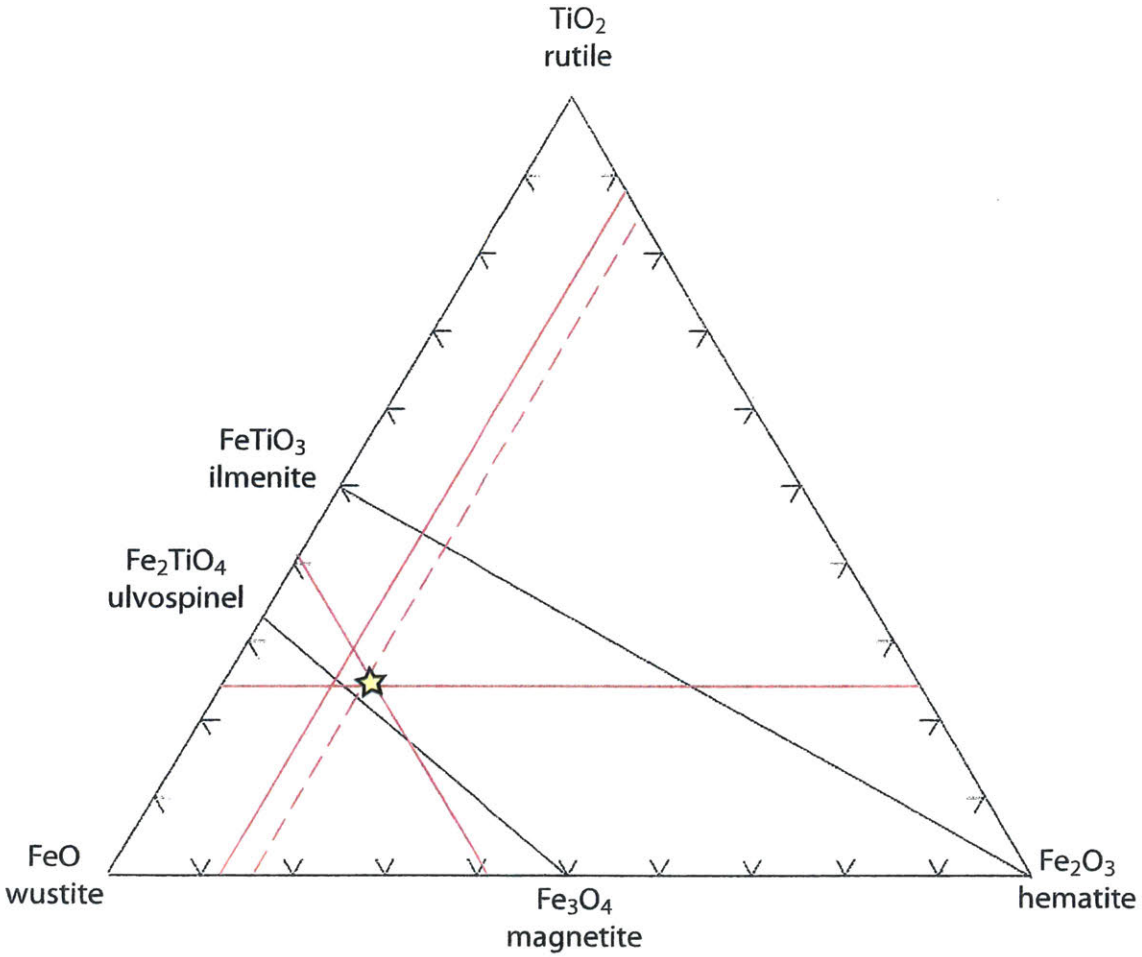

Figure 6: FeO-Fe_2O_3-TiO_2 Ternary diagram for the large grain, relatively common ferromagnetic mineral determined to have the formula $Fe_{2.26}Ti_{0.74}O_4$. The solid lines plot the percentages of FeO, Fe_2O_3 and TiO_2 seen in the atomic proportions of the mineral. The dashed line shows the proportion assuming that all the aluminum cations are impurities substituting for ferric iron. The yellow star at the intersection of these lines shows the inferred composition of the mineral.

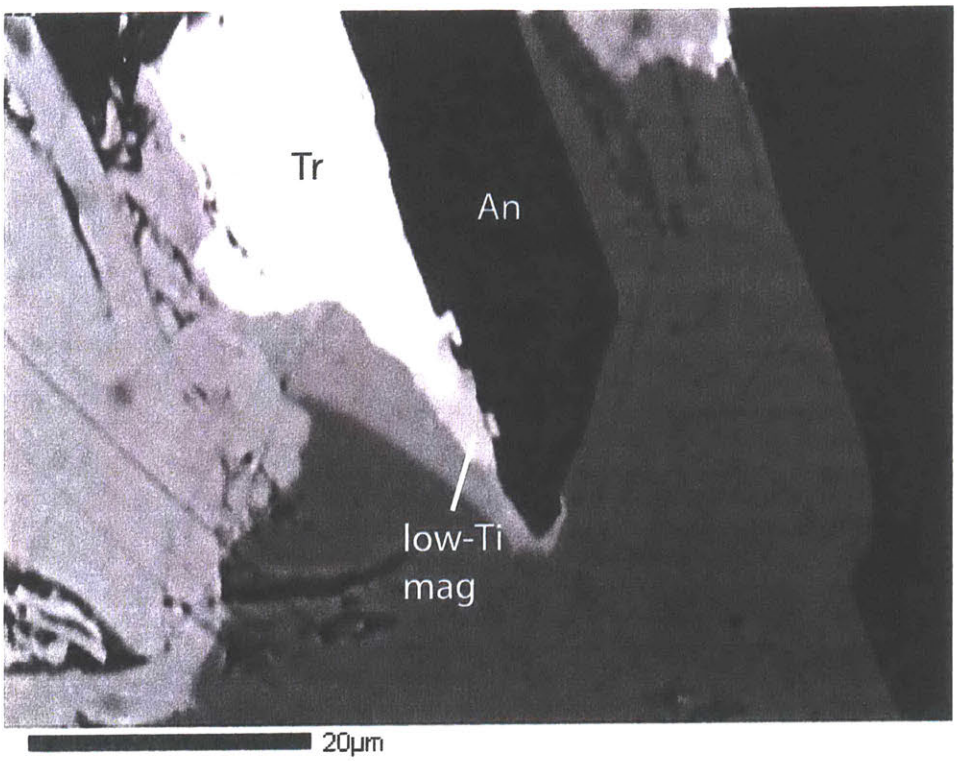

Figure 7: Backscatter electron microscopy imaging of SAH 99555,5b showing an example of the low-Ti ferromagnetic mineral found along the rims of some troilite grains. An = anorthite, Tr = troilite, low-Ti mag= low-Ti ferromagnetic mineral with formula here of $Fe_{2.66}Ti_{0.34}O_4$.

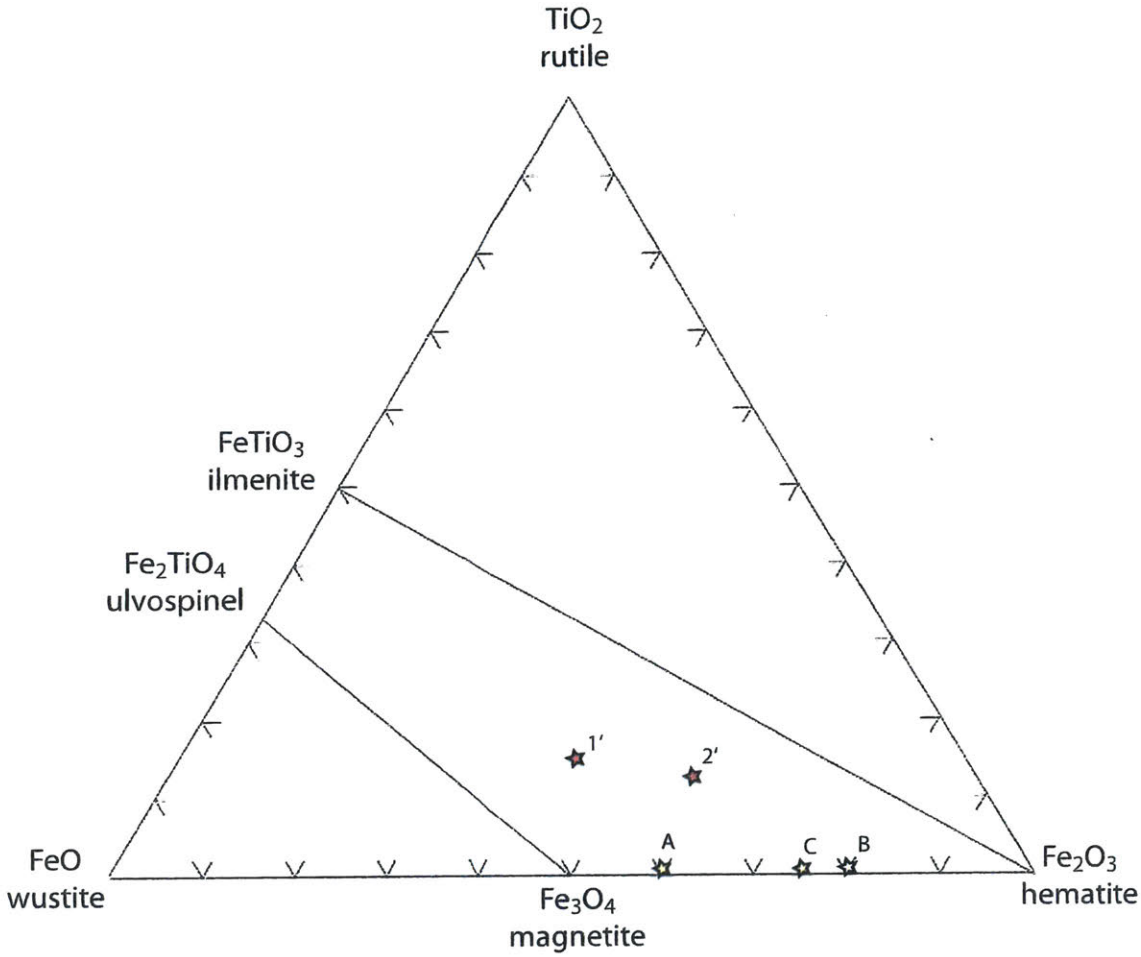

Figure 8: FeO-Fe_2O_3-TiO_2 ternary diagram for the less common ferromagnetic minerals with weight percents from Table 2. Grains 1' and 2', the red stars, were found around the rims of troilite (Fig. 7). Grains A, B, and C, the yellow stars, are unique in that they have little to no Ti or Al in them (Fig. 9).

A

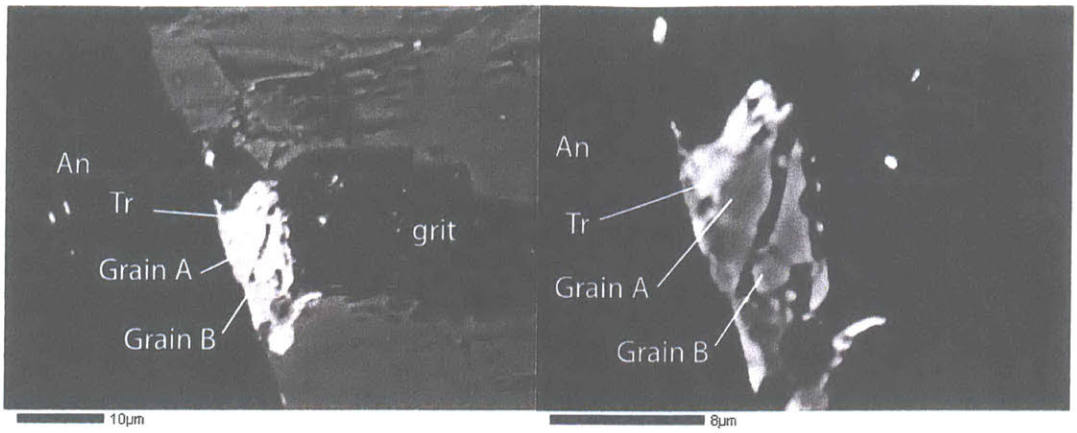

B

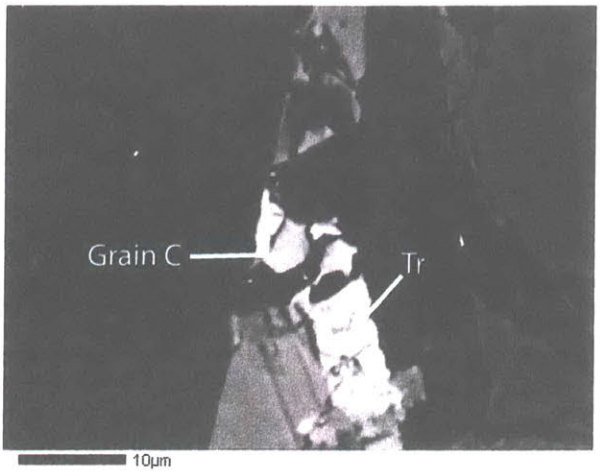

Figure 9: Backscatter electron microscopy imaging of SAH 99555,5b showing the three iron-oxide grains with little to no Ti and Al. (A) shows the same section containing both Grain A and B, just with two different magnitudes and contrasts. (B) shows the section with Grain C. An = anorthite, Tr = troilite, grit = poorly polished section with remnants of grit from the polishing paper

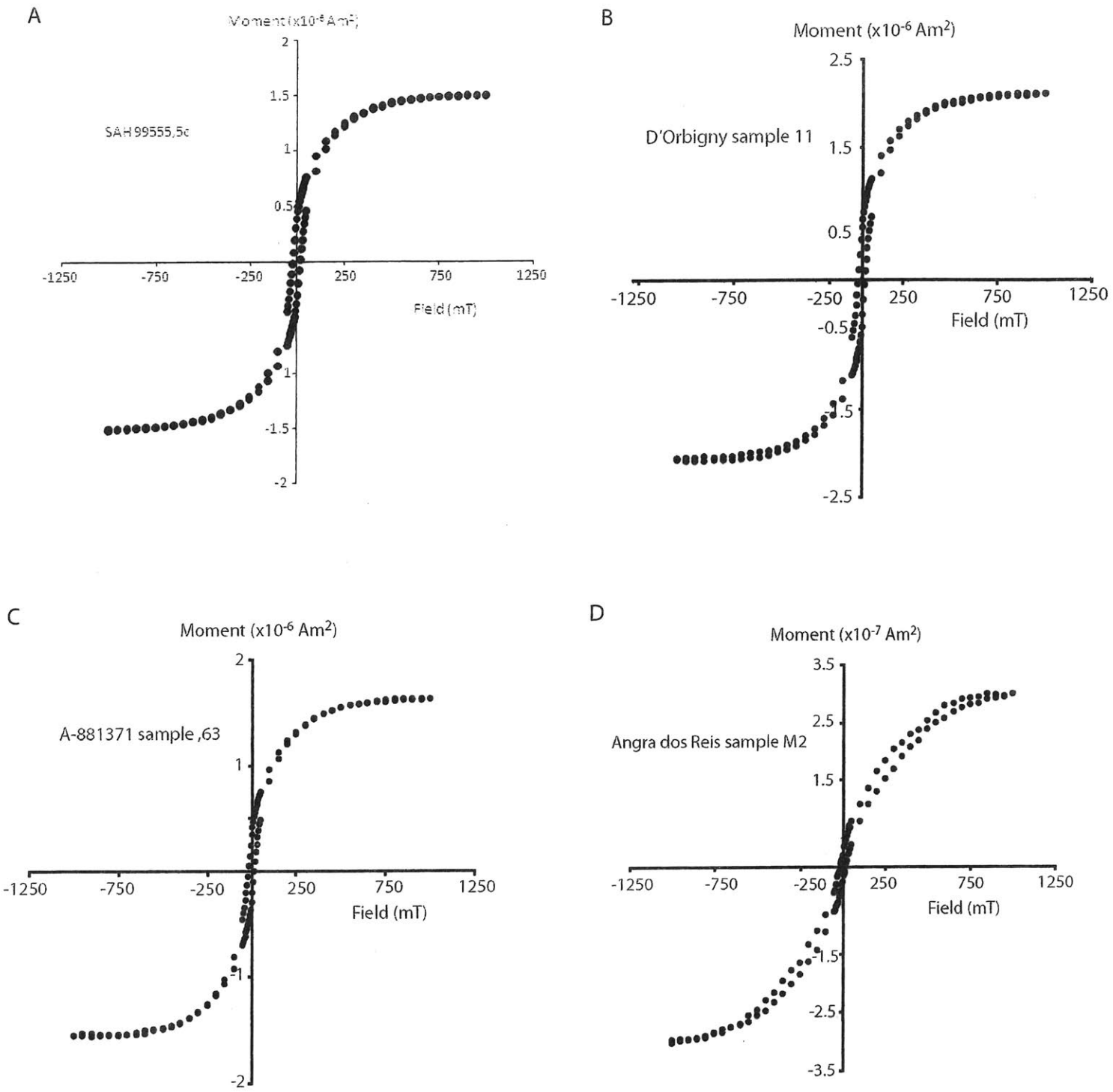

Figure 10: Room temperature hysteresis loops for SAH 99555,5b and samples from other angrites for comparison. The contribution from paramagnetic susceptibilty has been subtracted from all the data to form these figures. (B), (C), (D) are from Weiss et. al. 2008 *(4)*.

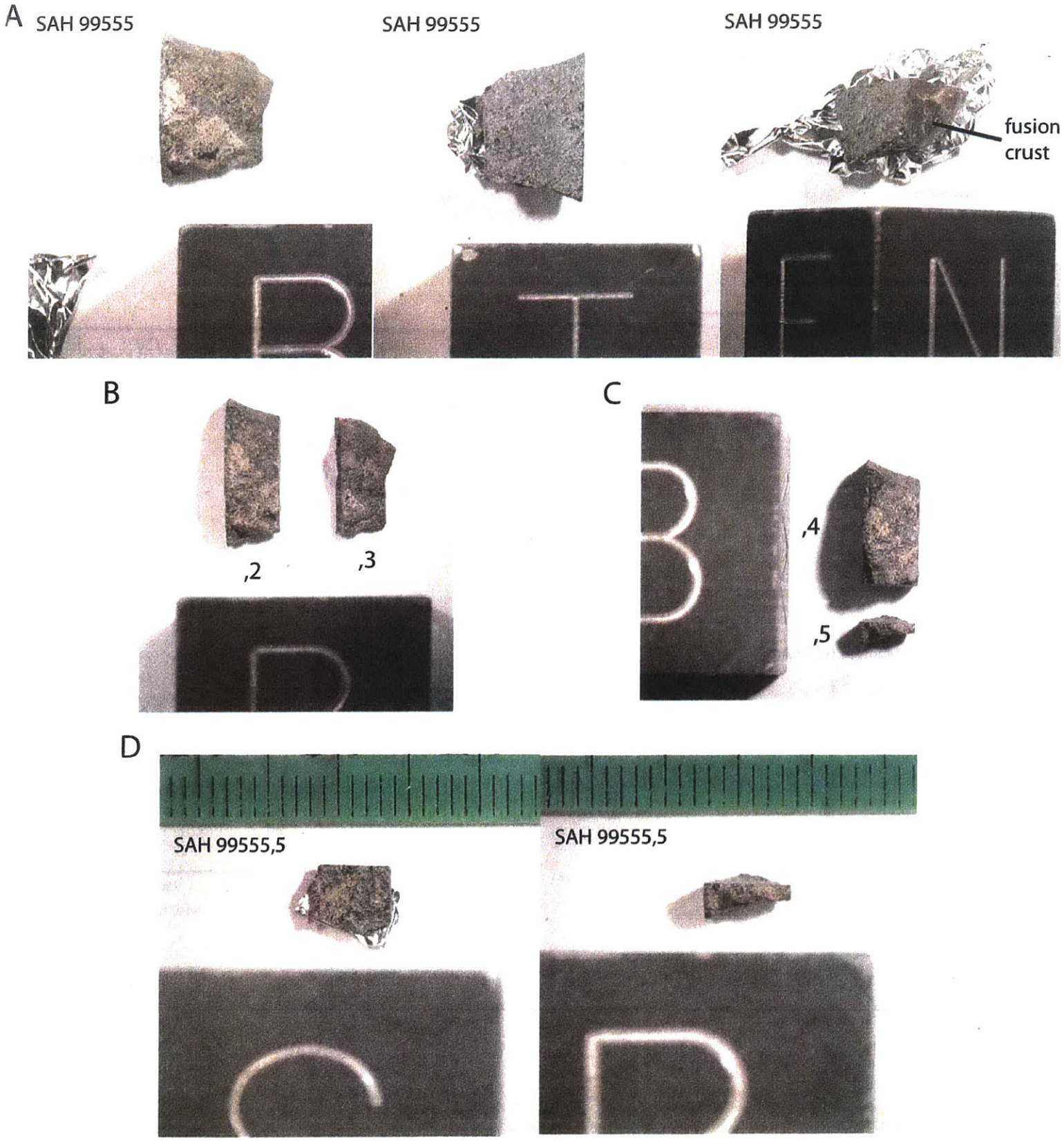

Figure 11: Photographs of SAH 99555. Direction of sample shown by black 1 inch cube. (A) shows the bottom, top and north-east faces of the sample as it was received. There are 2 cut surfaces (Top and East) which are close to perpendicular. The North face contains a portion of the fusion crust. (B) shows the first cut made on SAH 99555 to create subsamples ,2 and ,3. (C) shows the second cut which split SAH 995555,2 into subsamples ,4 and ,5. (D) shows the south and bottom face of SAH 99555,5. The green ruler is a mm scale.

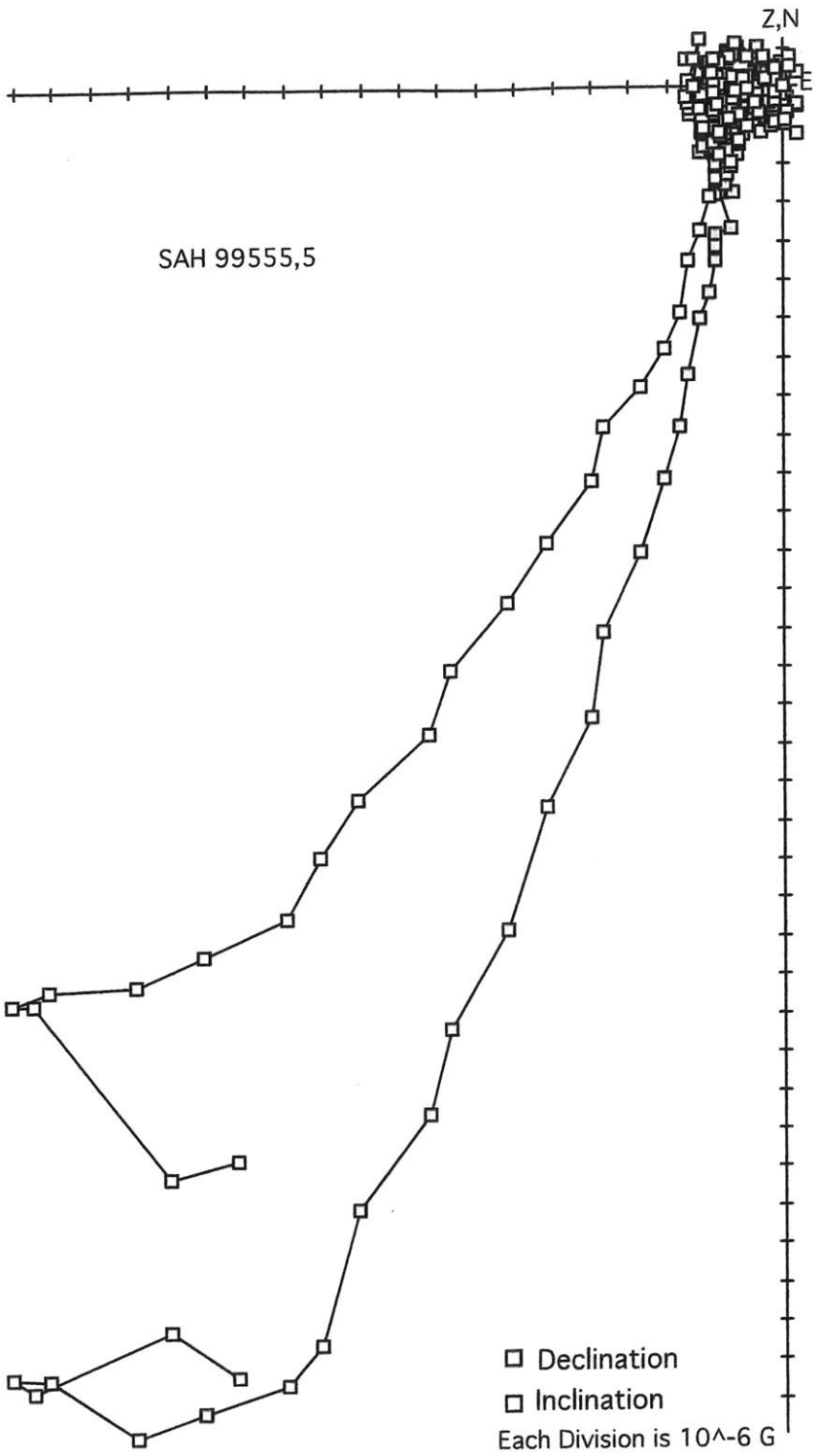

Figure 12: Orthographic plot of AF demagnetization of the NRM of SAH 99555,5 . It shows a two dimensional projection of endpoints of the NRM vector during AF demagnetization with a horizontal axis N-S-E-W plane and vertical axis plane (Z-D-E-W).

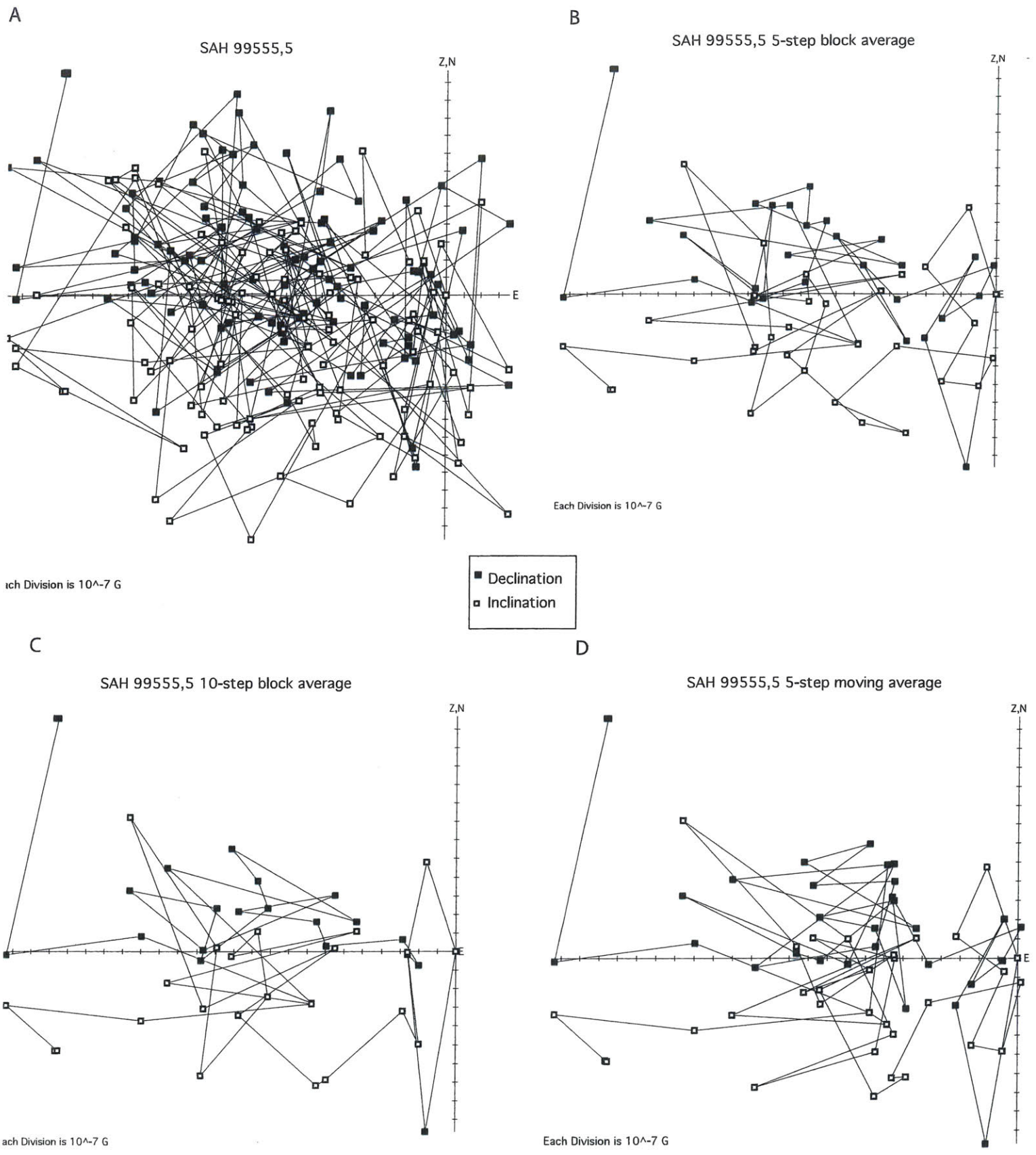

Figure 13: Comparison of averaging techniques applied to the higher-AF portion of the NRM of SAH 99555,5 . Here shown in an orthographic plot (a two dinmensional projection of endpoints of the NRM vector during AF demagnetization) with a horizontal axis N-S-E-W plane and vertical axis plane (Z-D-E-W). Here only NRM measurements for AF levels above 280 are shown. (A) shows the measurements for every step. (B), (C), (D) show the plot after the different averaging techniques were applied.

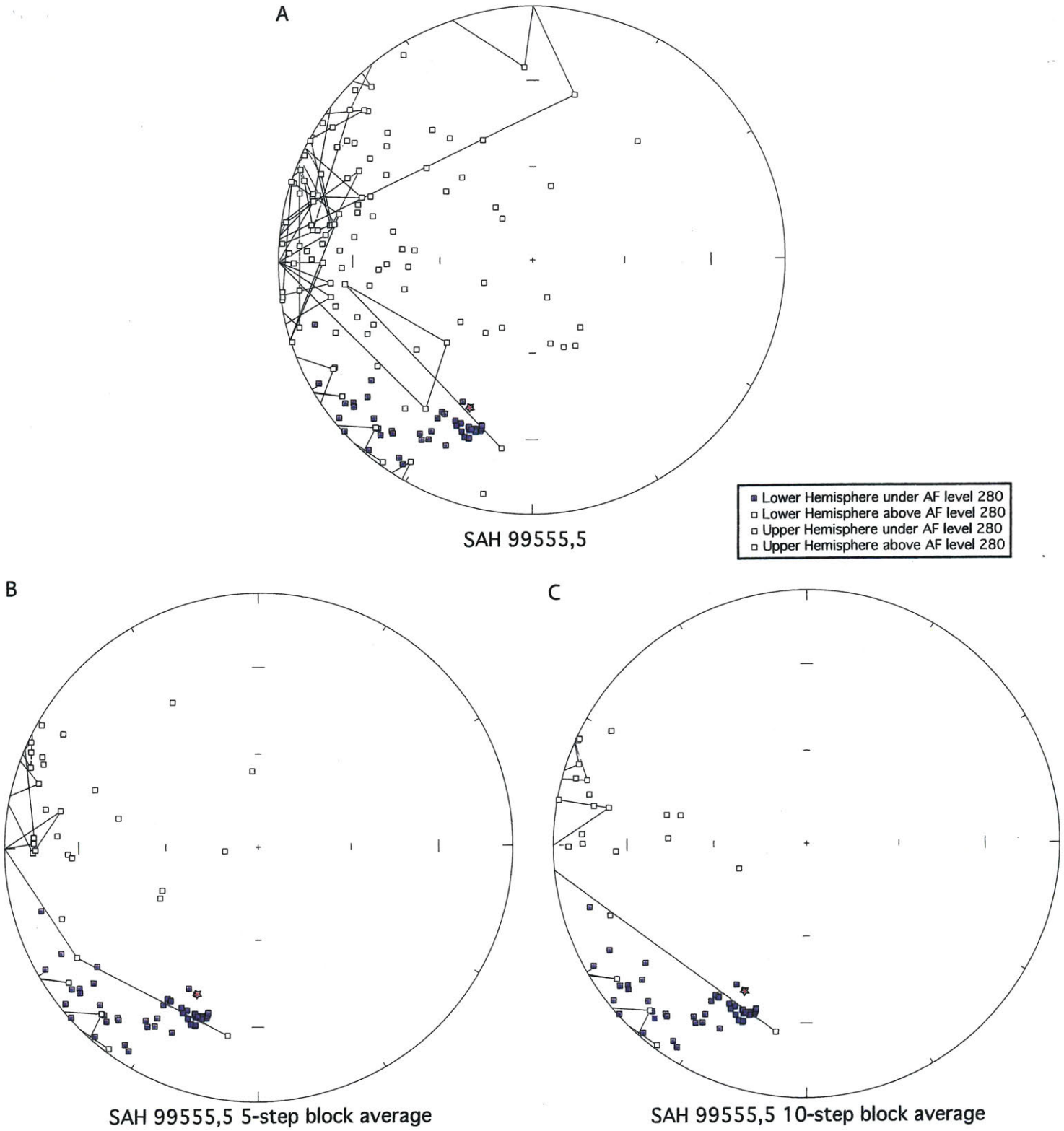

Figure 14: Comparison of equal area plots and the averaging techniques applied to the higher-AF portion of the NRM of SAH 99555,5 . Here shown in an equal area plot (a two dinmensional projection of endpoints of the NRM vector during AF demagnetization onto a sphere). NRM measurements for AF levels above 280 G are in light blue (lower hemisphere) and white (upper hemisphere) while those below AF level 280 G are in bright blue (lower hemisphere) and grey (upper hemisphere). A red star marks the NRM at the beginning of the AF demagnetization. (A) shows the measurements for every step. (B), and (C) show the plot after the 5-step and 10-step block averaging techniques were applied to the measurements for AF levels above 280 G.

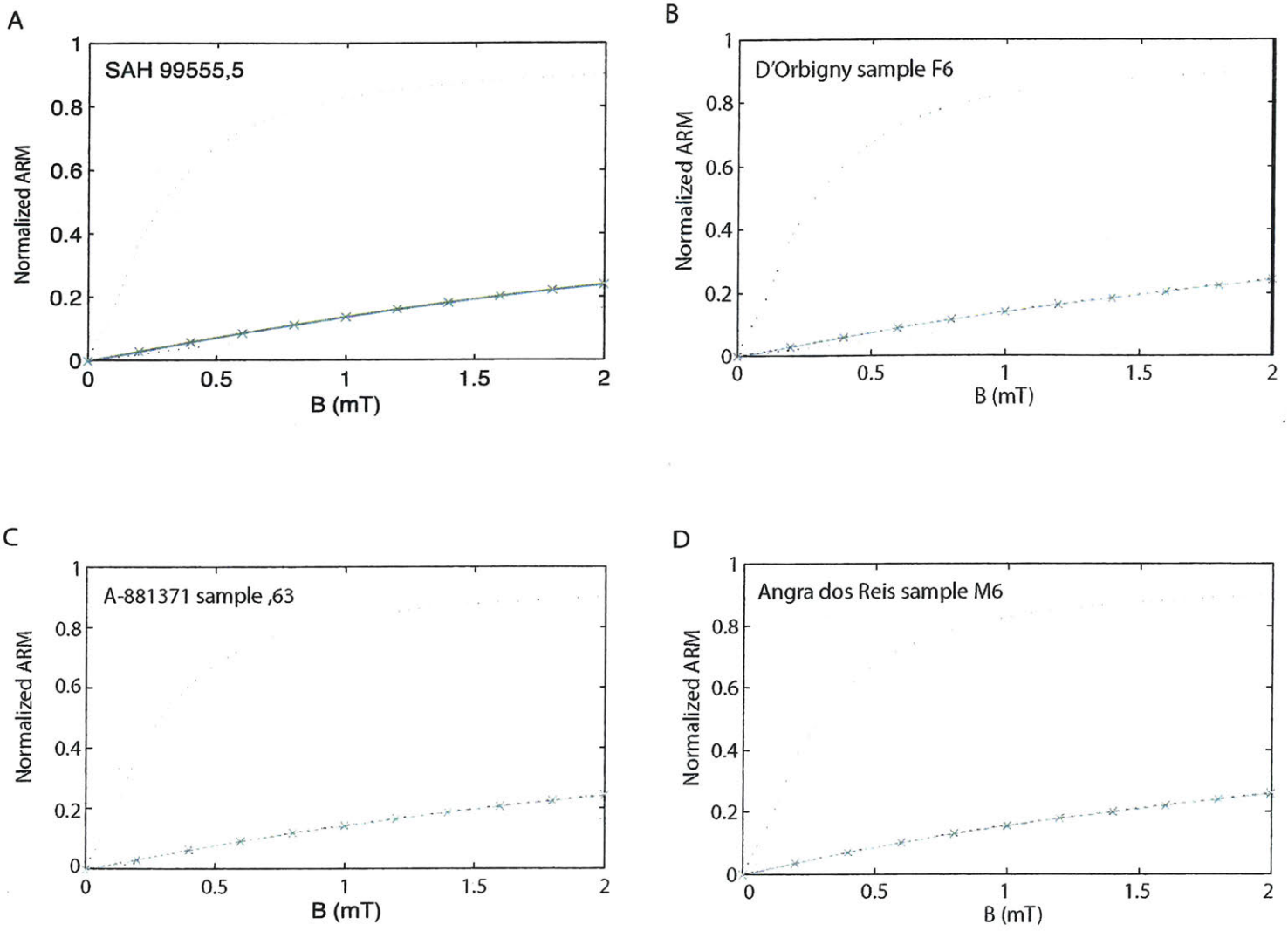

Figure 15: Plots of the ARM acquisition experiments on SAH 99555,5 and on characteristic samples of other angrites from Weiss et. al. 2008 *(4)*. The ARM results (green crosses) were acquired in a 2000 G AC field as a function of changing DC bias field (B). The lower red dotted curve is a highly-interacting chiton tooth magnetite and the upper blue dotted curve is that of a noninteracting magnetite from an magnetotactic bacteria which act as standards/boundaries for comparison.

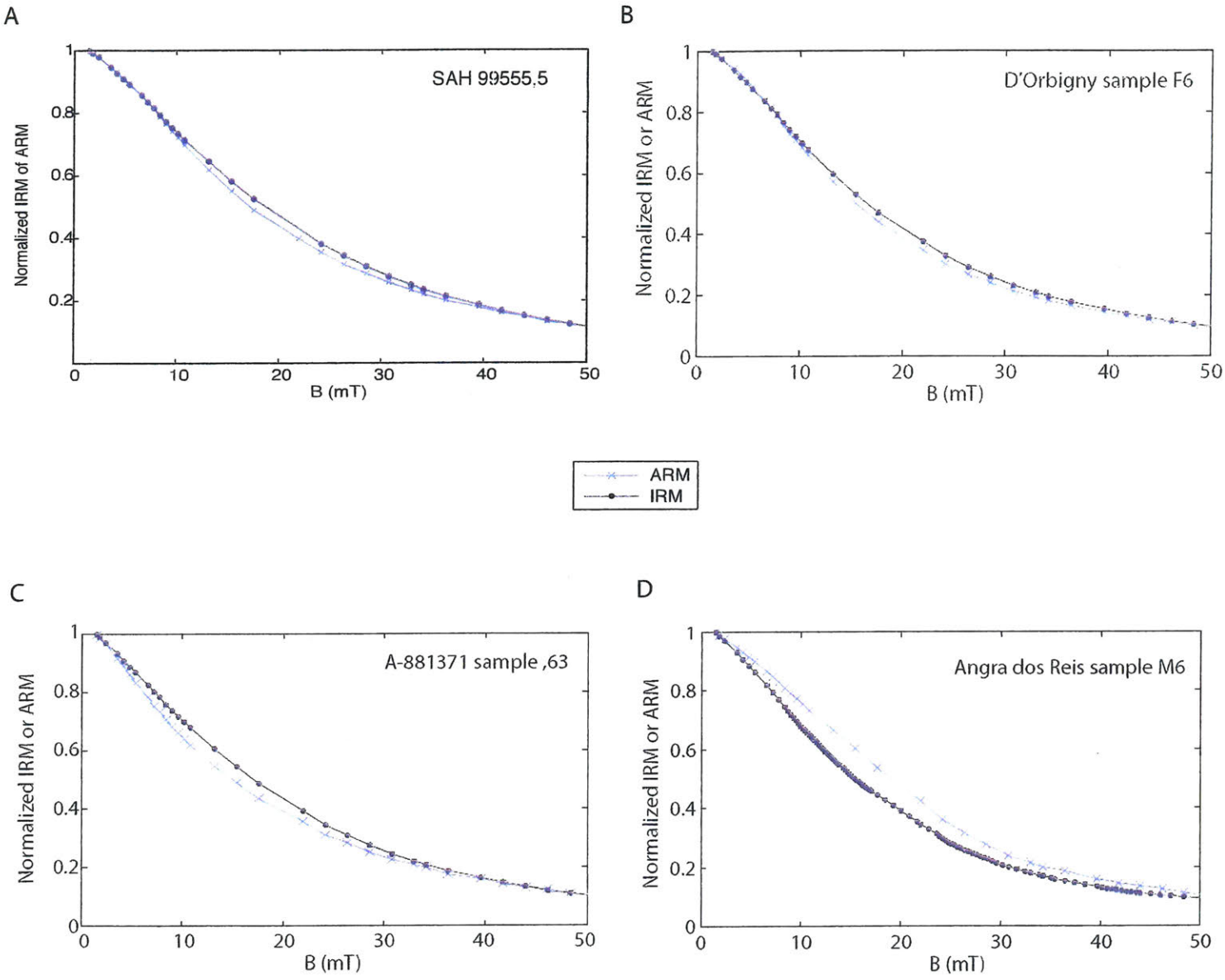

Figure 16: The Lowrie-Fuller test for SAH 99555,5 and on select samples of other angrites from Weiss et. al. (2008) *(4)*. The ARM data (light blue crosses) is the AF demagnetization of the ARM acquired in a 2000 G peak AC field with a DC bias field of 20 G. The IRM data (blue dots) is the AF demagnetization of the IRM acquired in a 2000 G field.

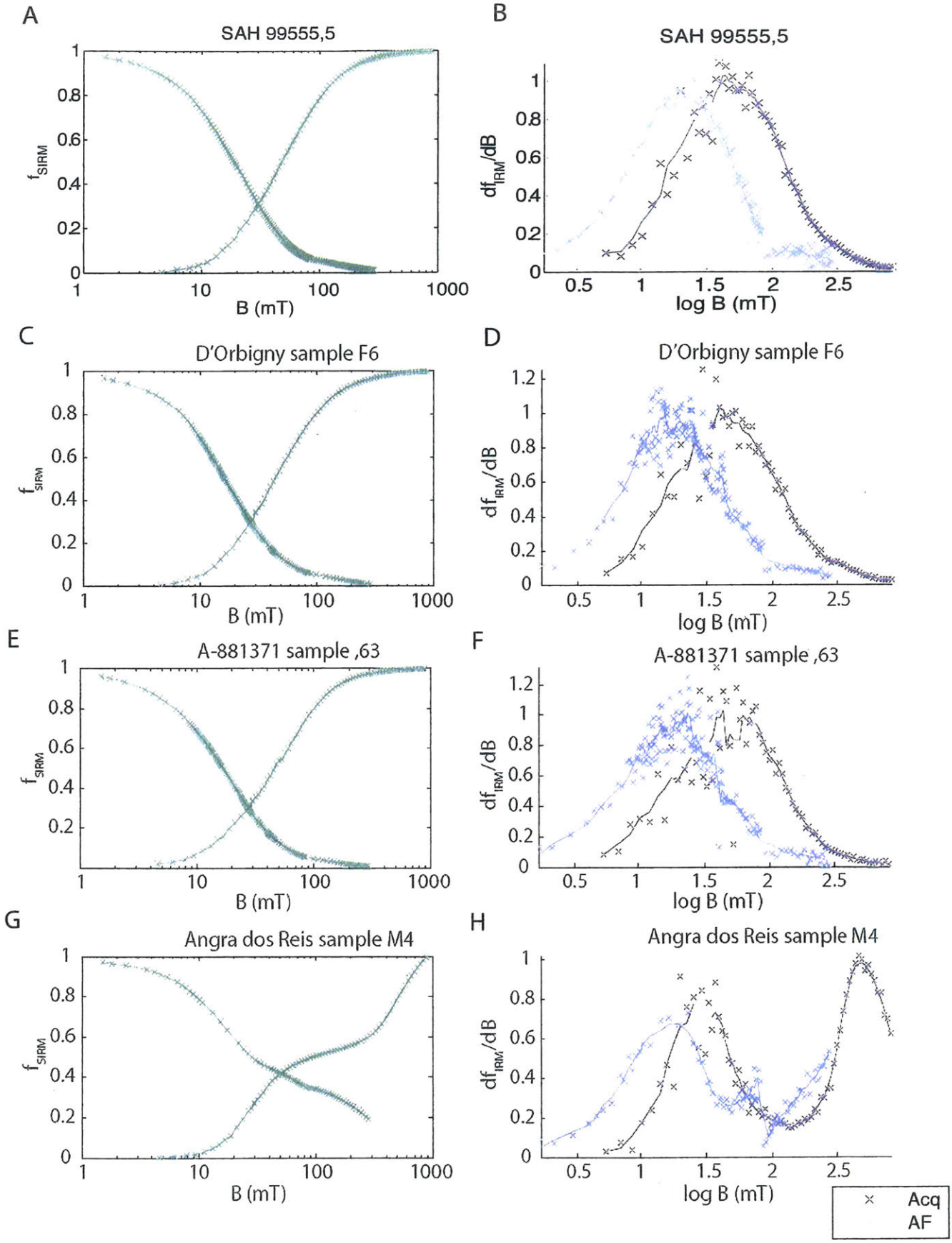

Figure 17: Plots of the IRM experiments on SAH 99555,5 and on select samples of other angrites from Weiss et. al. (2008) *(4)*. In (A), (C), (E), (G), the IRM acquisition and AF demagnetization of IRM are normalized to the highest-field IRM value. In (B), (D), (F), (H), the derivative of the IRM acquisition (purple crosses) is plotted against the AF demagnetization of the IRM (light blue crosses). The solid lines are running averages.

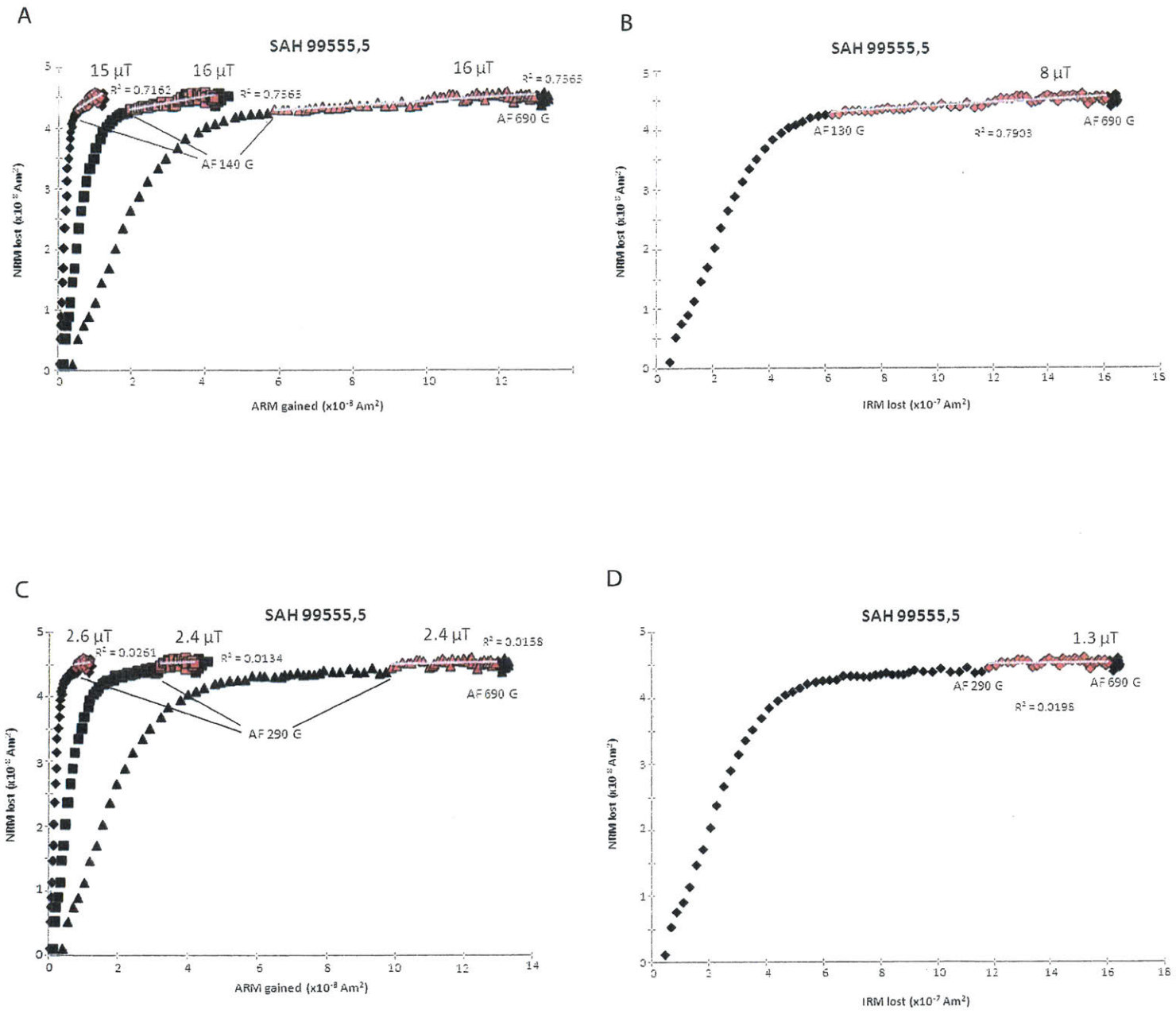

Figure 18: Paleointensity experiments on SAH 99555,5 with two different ranges selected. (A) and (C) are the ARM method where ARM gained while in a DC bias field of 0.5 G (diamonds), 2 G (squares), and 6 G (triangles) is plotted against NRM lost through AF demagnetization. (B) and (D) show the IRM method. The black symbols show the entire plot while the red ones are the ranges used for the paleointensity estimation. (A) and (B) uses AF levels from 130 G or 140 G to 690 G (above which the data is noisy) which appears to be the high-coercivity component by this visualization technique and where there are high R^2 values for the least squares fit. (C) and (D) use the range of AF levels 290 G to 690 G when the rotation of the sample had been stopped.

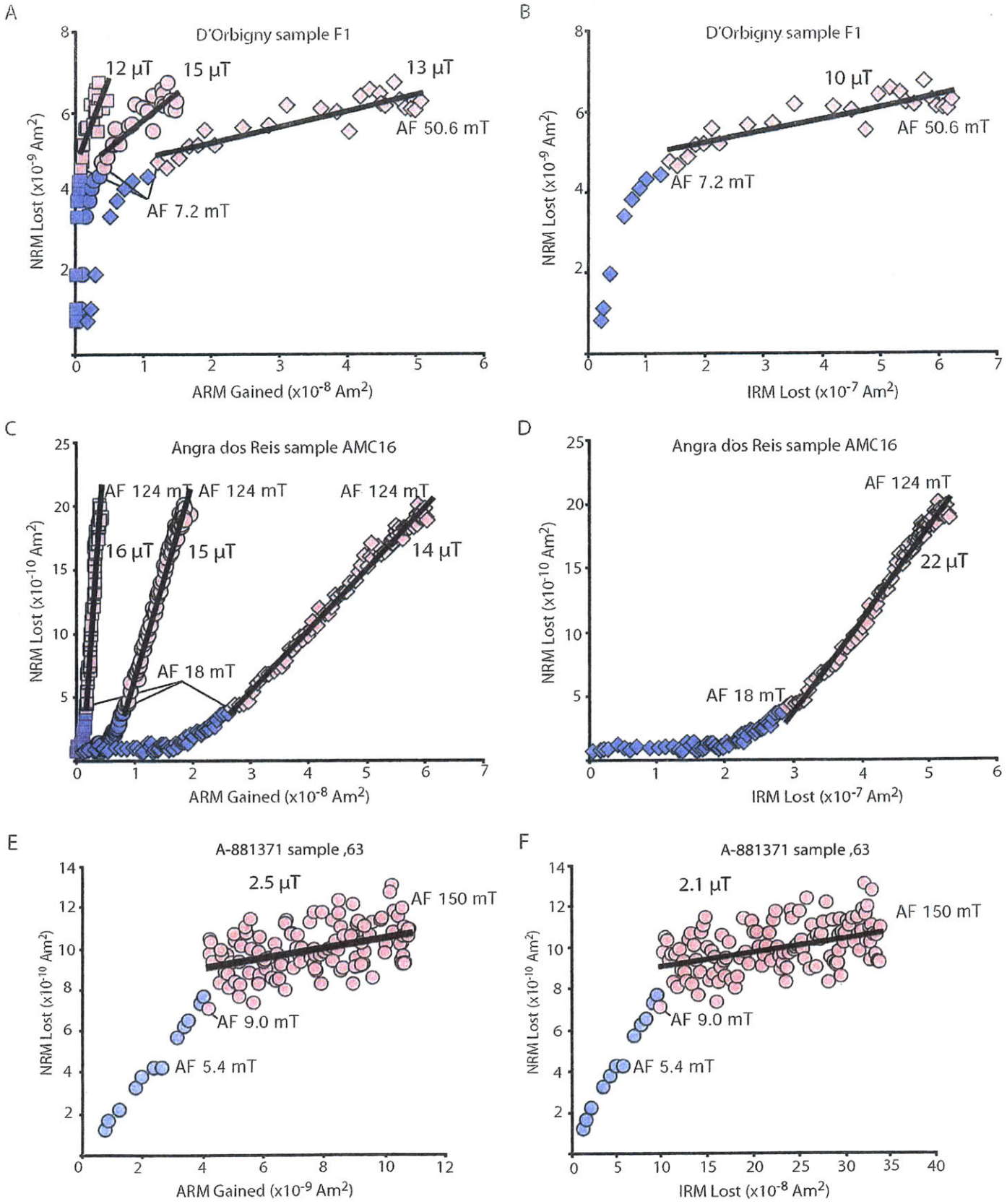

Figure 19: From Weiss et. al. 2008 *(4)*, paleointensity experiments on D'Orbigny sample F6, Angra dos Reis sample AMC16, and A-881371 sample ,63. (A), (C.), (E) show the ARM method where ARM gained while in a DC bias field of 0.5 G (squares), 2 G (circles), and 6 G (diamonds) is plotted against NRM lost through AF demagnetization. (0.5 G and 6 G not shown in A-881371 for clarity). (B), (D), (F) show IRM method. For D'Orbigny, data points from the low- coercivity component are blue, those from the high-coercivity component are red.